iScience

CellPress
OPEN ACCESS

Article

The evolutionary conserved iron-sulfur protein TCR controls P700 oxidation in photosystem I

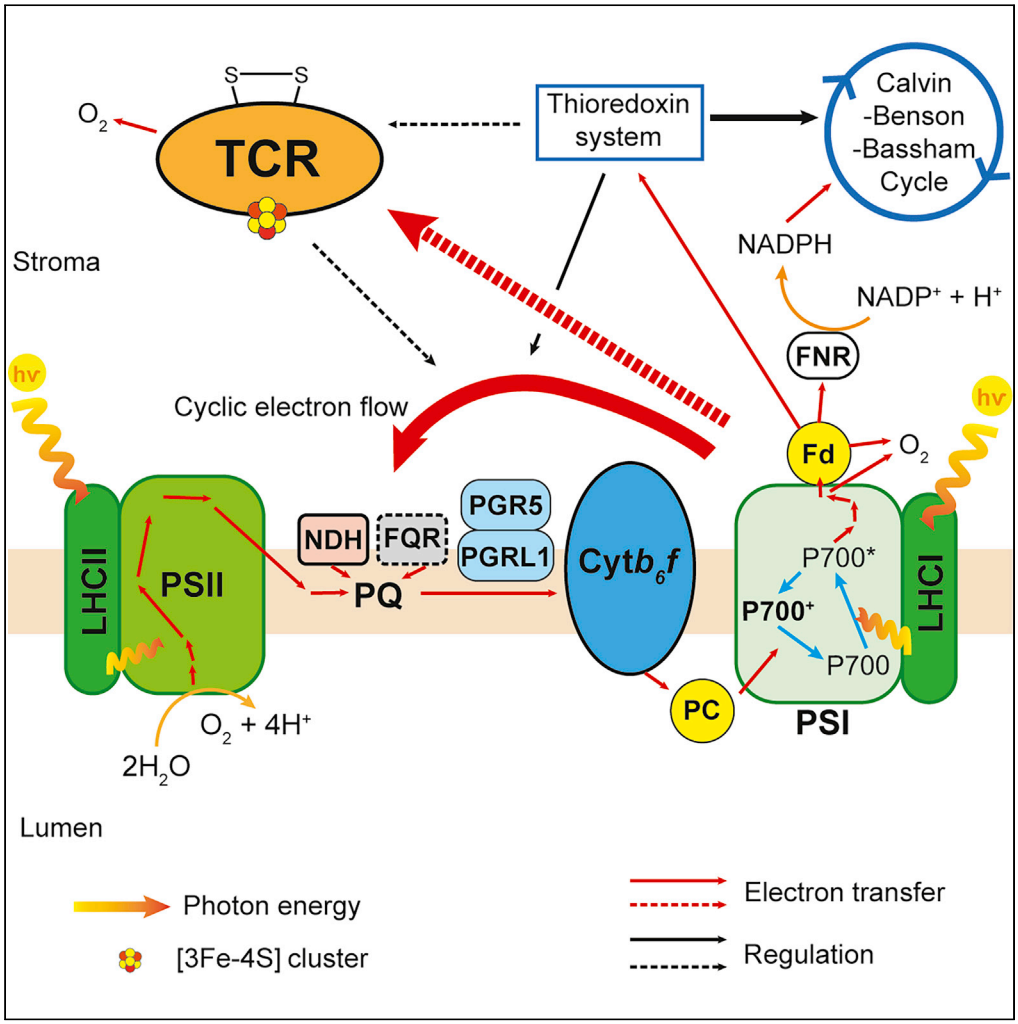

Mai Duy Luu Trinh, Daichi Miyazaki, Sumire Ono, ..., Hideki Taguchi, Toru Hisabori, Shinji Masuda

shmasuda@bio.titech.ac.jp

HIGHLIGHTS

P700 oxidation at photosystem I is important for regulation of photosynthesis

TCR is a redox active chloroplast protein harboring a 3Fe-4S iron-sulfur cluster

TCR controls electron flow around photosystem I, contributing to P700 oxidation

Luu Trinh et al., iScience *24*, 102059
February 19, 2021
https://doi.org/10.1016/j.isci.2021.102059

iScience

CellPress
OPEN ACCESS

Article

The evolutionary conserved iron-sulfur protein TCR controls P700 oxidation in photosystem I

Mai Duy Luu Trinh,[1] Daichi Miyazaki,[1] Sumire Ono,[1] Jiro Nomata,[2] Masaru Kono,[3] Hiroyuki Mino,[4] Tatsuya Niwa,[5] Yuki Okegawa,[6] Ken Motohashi,[6] Hideki Taguchi,[5] Toru Hisabori,[2] and Shinji Masuda[1,7,*]

SUMMARY

In natural habitats, plants have developed sophisticated regulatory mechanisms to optimize the photosynthetic electron transfer rate at the maximum efficiency and cope with the changing environments. Maintaining proper P700 oxidation at photosystem I (PSI) is the common denominator for most regulatory processes of photosynthetic electron transfers. However, the molecular complexes and cofactors involved in these processes and their function(s) have not been fully clarified. Here, we identified a redox-active chloroplast protein, the triplet-cysteine repeat protein (TCR). TCR shared similar expression profiles with known photosynthetic regulators and contained two triplet-cysteine motifs (CxxxCxxxC). Biochemical analysis indicated that TCR localizes in chloroplasts and has a [3Fe-4S] cluster. Loss of TCR limited the electron sink downstream of PSI during dark-to-light transition. *Arabidopsis pgr5-tcr* double mutant reduced growth significantly and showed unusual oxidation and reduction of plastoquinone pool. These results indicated that TCR is involved in electron flow(s) downstream of PSI, contributing to P700 oxidation.

INTRODUCTION

As an important component of life on Earth, plants and other photosynthetic organisms convert light energy to chemical energy through photosynthesis, which sustains almost all life activities on Earth (Blankenship, 2002). Photosystem (PS) II captures the photon energy to induce water splitting, and the electrons generated in this process are transferred sequentially to plastoquinone (PQ), cytochrome b_6f (Cyt b_6f), plastocyanin (PC), PSI, ferredoxin (Fd), and, finally, Fd-$NADP^+$ reductase (FNR), which reduces $NADP^+$ to NADPH (Govindjee et al., 2017). The electron transfer, called photosynthetic linear electron transfer (LET), generates NADPH and the proton-motive force across the thylakoid membranes that is required for ATP synthesis. NADPH and ATP are then used in the Calvin-Benson-Bassham (CBB) cycle to fix CO_2 (Blankenship, 2002).

After charge separation in the special pair of the chlorophyll dimer in PSI (P700), electrons are transferred to the primary electron acceptor A_0 followed by F_X, F_A, and F_B. The oxidized P700 is then re-reduced by PC (Blankenship, 2002). Fd receives electrons directly from F_B, which is the main electron transfer route downstream of PSI. When P700 is highly reduced due to the limitations of the electron transfer downstream of PSI, accumulated electrons produce reactive oxygen species (ROS), which damage iron-sulfur clusters (i.e., F_X, F_A, and F_B) and cause PSI photoinhibition (Tiwari et al., 2016). The PSI photoinhibition critically and negatively impacts plant growth, because it requires several days or weeks to replace the damaged PSI (Kudoh and Sonoike, 2002; Zhang and Scheller, 2004; Zivcak et al., 2015). Furthermore, the damaged PSI simultaneously induces PSII photoinhibition by downregulating the LET (Somersalo and Krause, 1989; Zhang and Scheller, 2004; Zivcak et al., 2015). Thus, maintaining a high level of $P700^+$ is essential in avoiding ROS generation and protecting PSI and PSII from photoinhibition. To date, several mechanisms involved in the P700 oxidation have been elucidated, including the downregulation of Cyt b_6f activity, chlororespiration, photorespiration, cyclic electron transfer (CET), and Mehler reaction (water-water cycle) (reviewed by Shimakawa and Miyake, 2018a).

The downregulation of Cyt b_6f activity is activated through the acidification of the thylakoid lumen (Nishio and Whitmarsh, 1993; reviewed by Tikhonov, 2013), and reduction of the PQ pool (Shaku et al., 2016;

[1]Department of Life Science and Technology, Tokyo Institute of Technology, Yokohama 226-8501, Japan

[2]Laboratory for Chemistry and Life Science, Institute of Innovative Research, Tokyo Institute of Technology, Yokohama 226-8501, Japan

[3]Department of Biological Sciences, Graduate School of Science, The University of Tokyo, Tokyo 113-0033, Japan

[4]Division of Materials Science (Physics), Graduate School of Science, Nagoya University, Nagoya 464-8602, Japan

[5]Cell Biology Center, Institute of Innovative Research, Tokyo Institute of Technology, Yokohama 226-8501, Japan

[6]Department of Frontier Life Sciences, Faculty of Life Sciences, Kyoto Sangyo University, Kyoto 603-8555, Japan

[7]Lead contact

*Correspondence: shmasuda@bio.titech.ac.jp

https://doi.org/10.1016/j.isci.2021.102059

Shimakawa et al., 2018). Nigericin-induced inhibition of luminal acidification leads to photoinhibition of 69% PSI and 29% PSII after a 20-min high-intensity light treatment (Joliot and Johnson, 2011), indicating that Cyt b_6f activity downregulation critically protects the photosystems from photodamage. Moreover, PQ pool reduction inhibits the Q-cycle in the Cyt b_6f (Shaku et al., 2016; Shimakawa et al., 2018). Once the Cyt b_6f activity is downregulated, the electron flow from Cyt b_6f to PC and then to the PSI acceptor side is limited, consequently suppressing electron donation to $P700^+$.

Chlororespiration is a light-independent O_2 consumption process in chloroplasts, wherein O_2 is reduced by electrons from PQ through the plastid terminal oxidase (PTOX) (Bennoun, 1982). Several studies on algae, *Ostreococcus* and *Chlamydomonas* elucidated the critical function of PTOX for photosynthetic regulation through P700 oxidation (Cardol et al., 2008; Houille-Vernes et al., 2011; Nawrocki et al., 2019a, 2019b, 2019c). However, the role of PTOX in land plants, including *Arabidopsis thaliana*, *Nicotiana tabacum*, and *Solanum lycopersicum*, is less clear, because PTOX over-expression causes increased light sensitivity (Ahmad et al., 2012; Heyno et al., 2009; Rosso et al., 2006). On another note, photorespiration, that is, the oxygenation of ribulose-1,5-biphosphate (RuBP) by RuBP carboxylase/oxygenase, plays a major role in maintaining P700 oxidation during a steady photosynthetic state (Cornic and Fresneau, 2002; Wada et al., 2018), because most PSI-derived electrons are transferred to FNR for NADPH formation for the CBB cycle and the photorespiratory pathway (Kannchen et al., 2020).

The CET is also critical for proper P700 oxidation. The CET was originally discovered by Arnon et al. as an electron transfer from the PSI acceptor side to the PQ pool through a putative Fd:PQ reductase (FQR) (Arnon et al., 1954). Together with the LET, the CET contributes to the pumping of H^+ from the stroma to the lumen in chloroplasts through Cyt b_6f, to generate the proton gradient across the thylakoid membranes (ΔpH) that is required for ATP synthesis as well as proper downregulation of the Cyt b_6f activity (reviewed by Munekage and Shikanai, 2005; Yamori and Shikanai, 2016). Using genetic approaches, PGR5 (Munekage et al., 2002), PGRL1 (DalCorso et al., 2008), and the NAD(P)H dehydrogenase-like (NDH) complex (Burrows et al., 1998; Shikanai et al., 1998) were identified as the main components of the CET chains (reviewed by Shikanai, 2007). Specifically, these components have been proposed to control two independent CET pathways including the PGR5/PGRL1-dependent CET (PGR-CET) and the NDH-complex-dependent CET (NDH-CET) (reviewed by Yamori and Shikanai, 2016). Nevertheless, there is a growing body of evidence even for functional models of the NDH-CET and the PGR-CET. Specifically, PGR5 was recently suggested to control P700 oxidation through regulation of the LET, but not CET (Takagi and Miyake, 2018). PGR5 and PGRL1 cannot fulfill efficient FQR activity (Nandha et al., 2007; Nawrocki et al., 2019a, 2019b, 2019c); the PGR5/PGRL1 complex has been proposed as an indirect regulator of CET (Joliot and Johnson, 2011; Nawrocki et al., 2019a, 2019b, 2019c). In fact, PGR5 does not contain any motifs to ensure an electron-transfer capability (Munekage et al., 2002). Regarding the NDH-CET, its contribution is very small because of the low NDH-complex:PSI stoichiometry (1:100) in C3 plants; therefore, the NDH-CET may not support the ΔpH formation and ATP synthesis required for CO_2 fixation (reviewed by Nawrocki et al., 2019a; 2019b; 2019c), although H^+ pumping rate in the complex has not been directly measured. Thus, the specific mechanisms underlying the CET chains still remain unclear, although the importance of CET for oxidation of P700 has been revealed.

Using a reverse-genetics screening, we identified a previously uncharacterized chloroplast redox-active protein, named triplet-cysteine repeat protein (TCR). TCR is a redox active [3Fe-4S] iron-sulfur cluster-binding protein localized in chloroplasts, and *tcr* mutant showed similar photosynthetic activity with those of the NDH complex mutant *ndho*, suggesting that TCR functions as an electron carrier involved in an alternative electron flow around PSI, which in turn controls the oxidation of P700.

RESULTS

Identification of TCR

We aimed to identify molecular components contributing to the precise regulation of photosynthesis in oxygenic phototrophs. Recently, with the development of rapid advanced technologies (e.g., microarrays and RNA sequencing), the gene expression status can be identified systematically in the interaction with other genes (van Dam et al., 2018). Genes showing similar expression profiles may be involved in similar biological processes; thus, co-expressed genes of known function(s) in a co-expressed gene network can provide insights into the functions of other genes with unknown function(s) (Eisen et al., 1998; Walker et al., 1999; Aoki et al., 2016). By use of the tools, we previously screened for *A. thaliana* genes that have the

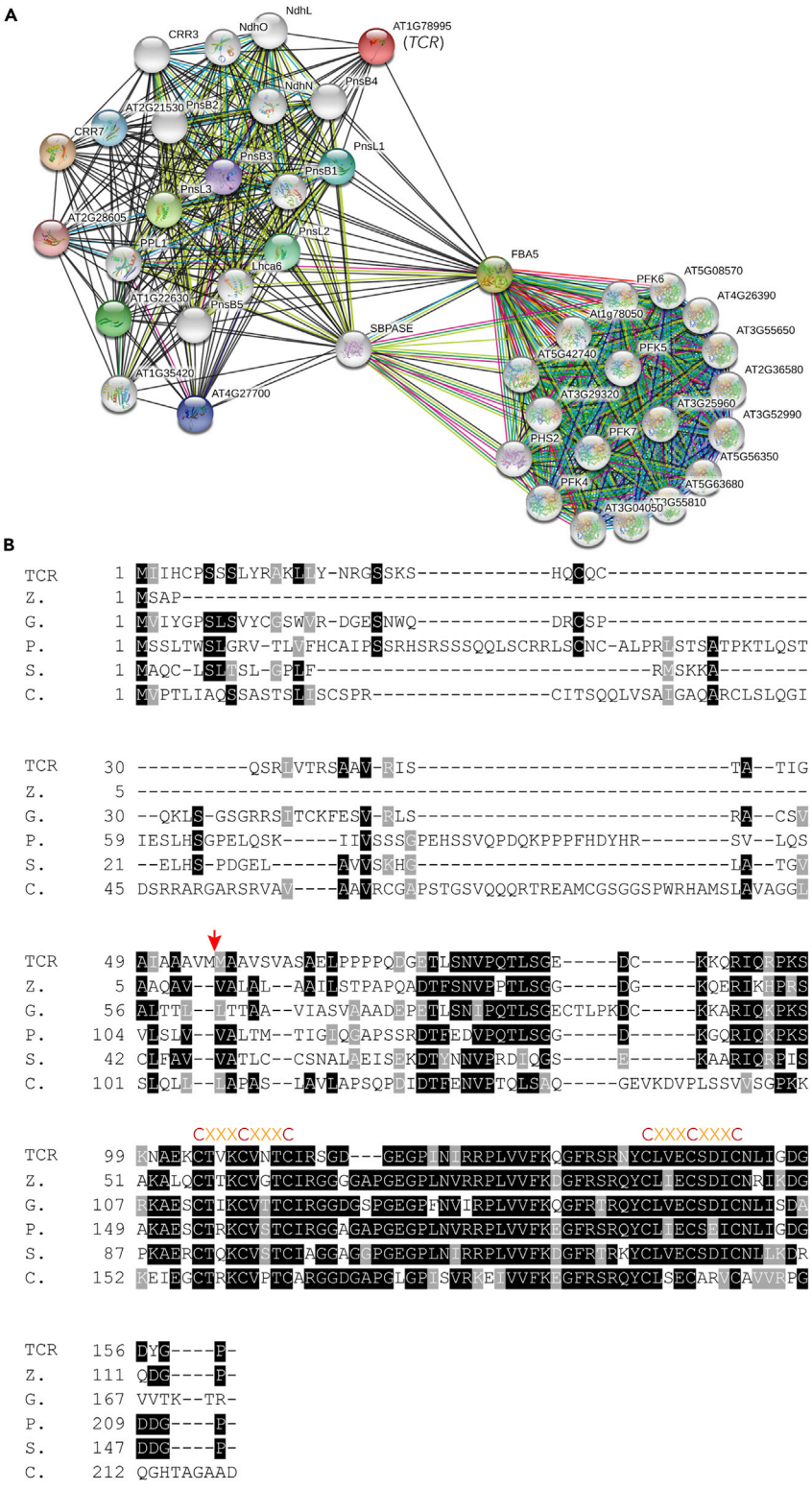

Figure 1. Identification of TCR by the reverse genetics screening

(A) TCR-related co-expression network. This network was built up by the STRING webserver (Szklarczyk et al., 2015).

(B) Deduced amino acid sequence alignment of the TCR homologs. The TCR homologs from *A. thaliana* (TCR), *Zea mays* (Z), *Glycine max* (G), *Physcomitrella patens* (P), *Selaginella moellendorffii* (S), and *Chlamydomonas reinhardtii* (C) were

Figure 1. *Continued*
aligned. The red arrow indicates the predicted cleavage site of the chloroplast-transit peptide. The alignment was done by the T-Coffee webserver (Di Tommaso et al., 2011; Notredame et al., 2000).
See also Figure S1.

following properties: (1) co-expressed with known photosynthetic regulatory genes, (2) predicted to encode a chloroplast protein, and (3) conserved among oxygenic phototrophs (Mai Duy Luu et al., 2018; Sato et al., 2017). In addition to FLAP1 (Mai Duy Luu et al., 2018; Sato et al., 2017) and DLDG1 (Harada et al., 2019), the details of which were reported previously by us, we here found another previously uncharacterized *Arabidopsis* gene at the open reading frame At1g78995 in a gene cluster in the STRING data resources (Szklarczyk et al., 2015), which include NDH-complex genes such as *NdhO*, *NdhL*, *NdhN*, *PnsB2*, *PnsB3*, *PnsB4*, *PnsB5*, *PnsL1*, *PnsL2*, *PnsL3*, *CRR3*, and *CRR7* (Figure 1A). This gene, abbreviated as *TCR*, encodes a small protein (159 amino acids) with an N-terminal predicted plastid-transit peptide, as assessed using the ChloroP server (Emanuelsson et al., 1999) (Figure 1B); the gene product was detected in the chloroplast fraction as examined by proteomics analysis of *A. thaliana* (Ferro et al., 2010). Based on the ATTED-II database (Aoki et al., 2016), *TCR* is co-expressed with *NPQ1* (which encodes violaxanthin de-epoxidase), NDH-complex genes (*PnsL3*, PnsB3, *CRR7*, and *CRR42*), carbohydrate metabolic pathways (FBA5 and FBA7), and Fd-dependent electron transfer genes (*FTRA2* and *FNR2*). The amino acid sequence alignment of TCR homologs (Figure 1B) and a phylogenetic tree of TCR (Figure S1) showed that TCR was specifically conserved in the photosynthetic green lineage, which includes green algae, liverworts, ferns, monocots, and dicots, but not found in red algae and cyanobacteria. Note that the amino acid sequence of TCR does not show any similarity to known proteins, such as Fds.

Among the TCR homologs, amino acid sequence similarities were higher at the C terminus versus the N terminus (Figure 1B). More strikingly, we identified an evolutionarily conserved triplet cysteine motif (CxxxCxxxC) that was repeated twice near the C terminus of the protein (Figure 1B). According to the structural prediction server Phyre2 (Mezulis et al., 2015), TCR secondary structure contains five helices, and the two helices contain the triplet cysteine motifs with high confidence (Figure S2A). The Phyre2 could not predict a reliable tertiary structure of TCR, because no similar protein to TCR was identified in the protein databank (PDB) library (Bairoch et al., 2005). Hence, *ab initio* modeling QUARK (Xu and Zhang, 2012, 2013) was utilized to build the predicted tertiary structure of TCR. Top five obtained models of TCR structure showed that two triplet cysteine motifs positioned in two distinct helices (Figure S2B), which is consistent with the data obtained by Phyre2 (Figure S2A), and a disulfide bond was formed between the two helices of the first obtained model of TCR structure (Figure S2B). The remaining four cysteine residues of this predicted model (Figure S2B) seemed to coordinate an iron-sulfur cluster, as shown in several iron-sulfur proteins designed *de novo* (Dizicheh et al., 2017; Nanda et al., 2016); however, in most cases, the iron-sulfur cluster(s) is bound in loop region(s) in natural proteins. These unique characteristics of TCR prompted us to proceed with the characterization of TCR function in relation to photosynthetic regulation.

TCR is an iron-sulfur protein

The N-terminal His-tagged TCR from *A. thaliana* was expressed in *Escherichia coli*, and purified by Ni-affinity resin under anaerobic conditions (Figure 2A). Under anaerobic conditions, purified TCR had a dark-brown color (Figure 2B), which was not clearly observed for TCR purified under ambient air (data not shown) indicating that TCR might be a ligand-binding protein and the ligand might be sensitive to ambient air (containing ~21% O_2). In fact, the loss of dark-brown color was accompanied by the aggregation and precipitation of purified protein. The absorption spectrum of TCR had a broad peak at 420 nm (Figure 2C), which is a typical feature of iron-sulfur-cluster-binding proteins (Freibert et al., 2018; Hoppe et al., 2011; Kennedy et al., 1984; Li et al., 2019; Nakamaru-Ogiso et al., 2002; Yabe et al., 2004). The 420 nm absorption (A_{420}) is attributed to ligand-to-metal (Cys-S/Fe^{2+}) charge transfer in the iron-sulfur clusters (Hoppe et al., 2011; Lippard and Berg, 1994), suggesting that TCR binds an oxygen-sensitive iron-sulfur cluster. The absorption spectrum of oxidized TCR is similar to those of iron-sulfur proteins containing a [4Fe–4S] or [3Fe–4S] cluster (Hoppe et al., 2011; Ibrahim et al., 2020; Lippard and Berg, 1994; Nakamaru-Ogiso et al., 2002). Dithionite reduces TCR, which results in decreased A_{420} (Figure 2C, blue line) and diminished color intensity (Figure 2B). In contrast, A_{420} was modestly increased by the 1-min exposure to ambient air (Figure 2C, dashed red line), indicating that most of the purified TCR contained an oxidized iron-sulfur cluster and that the remaining reduced form can be oxidized by O_2. Given that we expressed TCR in aerobically grown *E. coli*, the iron-sulfur cluster in the expressed TCR was oxidized in *E. coli* cells, although it is labile to ambient air after breaking the cells.

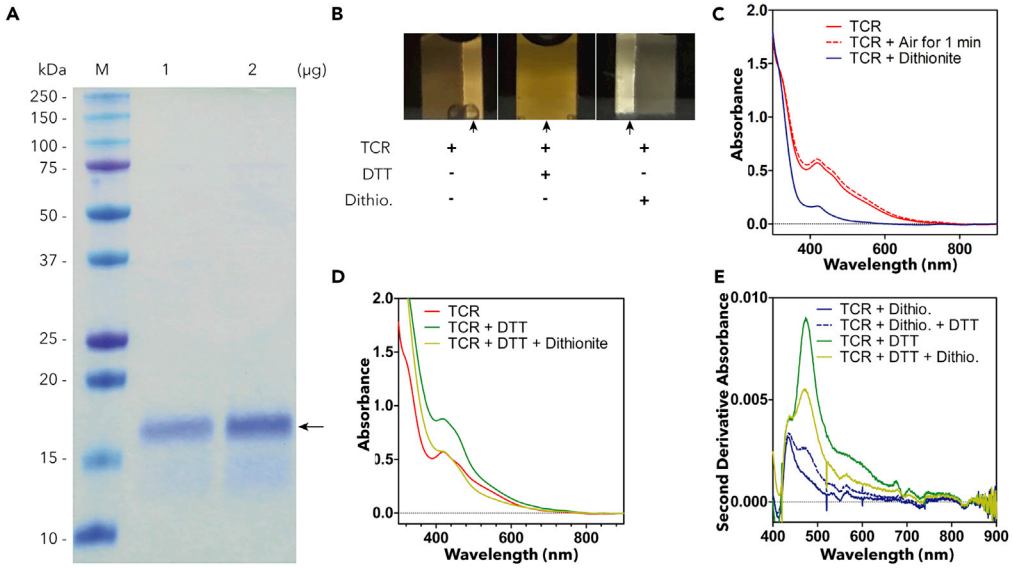

Figure 2. Biochemical properties of TCR

(A) SDS-PAGE profile of the purified TCR expressed in *E. coli*. The arrow indicates the His-tagged TCR band.

(B) Color change of the purified TCR by oxidation and reduction of a disulfide bond and a putative iron-sulfur cluster. The black arrows indicate specific positions showing color change. Dithio, dithionite.

(C) Absorption spectra of purified TCR in the presence and absence of dithionite. Spectra were acquired under anaerobic conditions, with the exception of that of TCR exposed to ambient air for 1 min.

(D) Absorption spectra of purified TCR in the presence and absence of dithionite and/or DTT. Spectra were acquired under anaerobic conditions.

(E) Second-derivative absorption spectra of the spectra shown in (D) and (E). Dithio, dithionite.

Next, we treated TCR with dithiothreitol (DTT) under anaerobic conditions. In contrast to dithionite that specifically reduced iron-sulfur clusters in proteins without reducing disulfide bonds (Yin et al., 2013), DTT can efficiently reduce disulfide bonds and iron-sulfur clusters having relatively high redox potentials (Daltrop et al., 2002). Strikingly, the visible TCR spectrum absorption was increased by DTT treatment (Figure 2D, green line), accompanied by the appearance of a new peak at 480 nm, as clearly observed in the second-derivative absorption spectrum (Figure 2E, green line), indicating that the iron-sulfur cluster in TCR could not be reduced by DTT (−0.33V), and its absorption property was altered, possibly, due to breakage of the disulfide bond near the cluster (Figure S2B). As expected, adding dithionite to the DTT-treated TCR resulted in decreased levels of both A_{420} and A_{480} due to the reduced iron-sulfur cluster (Figures 2D and 2E, yellow lines). Notably, DTT addition to the dithionite-reduced TCR induced an increased A_{480}, but not A_{420} (Figure 2E, dashed blue line), supporting the hypothesis that the increased A_{420} and the appearance of A_{480} upon DTT treatment (Figure 2D) may have resulted from TCR's conformational change through the breakage of a disulfide bond (Figure S2B). The A_{420} to A_{280} ratios of purified TCR with or without DTT were 0.35 and 0.22, which were a little smaller than those of other reconstituted [3Fe–4S] iron-sulfur proteins (0.3–0.4) (Ibrahim et al., 2020), suggesting that the purified sample contained a certain amount of apo-proteins.

To determine the structure of the iron-sulfur cluster in TCR, electron spin resonance (ESR) measurements were conducted with purified TCR. Air-oxidized TCR showed an ESR signal at g = 2.028, which is a typical feature of the electronic spin state (S = 1/2) of irons in oxidized [3Fe–4S] clusters (Figure 3A) (Ibrahim et al., 2020; Surerus et al., 1989; Telser et al., 2000). This signal must have originated from the metal center, because the ESR signal was not saturated at high microwave powers at cryogenic temperature (Figure 3B). In other words, the recorded ESR signal, herein, reflects the status of the electron spin of irons in the iron-sulfur cluster. Notably, the symmetrical ESR spectrum of TCR (Figure 3A) indicated the small g-anisotropy, which suggests that three Fe ions are located in a symmetrical coordinate. Given that a reduced [3Fe–4S] is ESR-silent (Telser et al., 2000), the weaker ESR signal observed in the dithionite-treated TCR sample (Figure 3A) indicated that dithionite cannot fully reduce TCR. In fact, the absorption spectrum of the

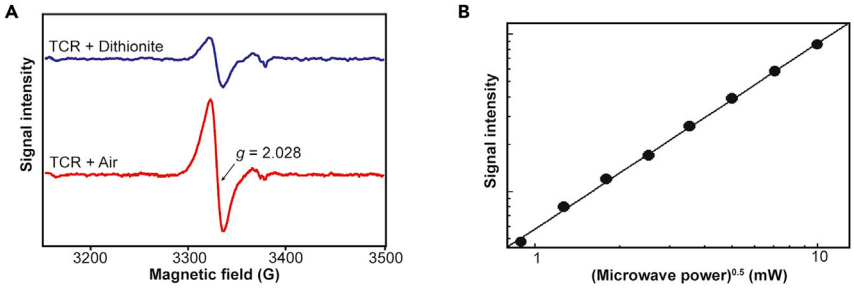

Figure 3. ESR spectra of the TCR recombinant protein

(A) ESR spectra of the oxidized (red) and reduced (blue) TCR. Microwave frequency, 9.46 GHz. Microwave power, 100 mW. Field modulation, 4G. Temperature, 6K.

(B) The microwave power saturation the ESR signal of the oxidized TCR. Microwave frequency, 9.46 GHz. Field modulation, 4G. Temperature, 6K.

dithionite-treated TCR sample still had a small absorption peak at 420 nm (Figure 2C). This raised a possibility that TCR has a very low redox-potential and cannot be completely reduced by dithionite.

TCR localizes in chloroplast

To determine whether TCR localizes in chloroplasts, as predicted by ChloroP (Emanuelsson et al., 1999), we transiently expressed the recombinant green fluorescent protein (GFP) fused with a predicted signal peptide of TCR (64 N-terminal amino acids) in onion epidermal cells. The recombinant GFP was localized in plastids, as observed for the plastid-localizing control CYO1-GFP (Shimada et al., 2007), but not for the negative control (*GFP* alone) (Figure 4A), indicating that the N terminus of TCR functions as the plastid-signaling peptide. We also expressed GFP fused with the full-length TCR in *A. thaliana* using the *35S* promoter of the cauliflower mosaic virus and found that GFP fluorescence overlapped with chlorophyll autofluorescence in mesophyll chloroplasts (Figure 4B), indicating that mature TCR localizes in chloroplasts.

Next, we characterized the localization of TCR at the sub-organelle level. Unfortunately, anti-TCR antibodies used for immunoblotting cannot be produced, although six trials to produce anti-TCR were achieved with short peptides and full-length TCR. Alternatively, we used the TCR-GFP-expressing line to characterize the sub-cellular localization. We isolated total chloroplasts from the transgenic *A. thaliana* plants expressing *TCR-GFP* described above and separated them into the thylakoid membrane and soluble fractions. To obtain the membrane fractions, thylakoid membranes were washed with a low-osmotic buffer four times, followed by the confirmation that most soluble proteins, including the Rubisco large subunit (RbcL), were washed out (Figure 4C). Notably, the thylakoid membranes were broken in the low-osmotic washing buffer, so that the soluble proteins in the lumen were also washed out. Although we detected TCR-GFP mostly in soluble fractions, a small amount of TCR-GFP was detected in membrane fractions, even after the four washing steps, suggesting that TCR localizes in both thylakoid membranes and soluble fractions, as observed for the PSII-associated protein PSBO (Figure 4C). The washed thylakoid membranes were then treated with different salts and analyzed using western blotting. We used chaotropic salt solutions containing 2 M NaBr or 2 M NaSCN for disrupting the hydrogen bonding network between water molecules and weakening the hydrophobic effect within and/or between protein molecules. Alkaline solution (0.1 M Na_2CO_3) will affect ionic bonds within and/or between protein molecules and the stability of lipid bilayer membranes. Signal intensity of membrane-bound TCR-GFP was increased after NaBr, NaSCN, or Na_2CO_3 treatment perhaps due to the reduction of overlapped proteins on the polyvinylidene difluoride (PVDF) membranes. The relative amount of TCR-GFP in soluble fractions, compared with those in membrane fractions, was clearly increased after the salt treatment (Figure 4D). A similar phenomenon was observed for PSBO. The thylakoid-membrane-spanning PSII subunit D1 was stably maintained in the thylakoid membrane fractions. Taken together, these data demonstrated that TCR is soluble, some of which associate with thylakoid membranes, probably, via an interaction with an unknown membrane protein or complexes; this finding is consistent with a previous proteomics analysis of *A. thaliana* chloroplasts that showed that TCR was present in the isolated thylakoid membranes (Ferro et al., 2010). High accumulation of TCR-GFP in soluble fractions may have resulted from higher TCR-GFP expression than that of the endogenous TCR, resulting in TCR binding site saturation on thylakoid membranes.

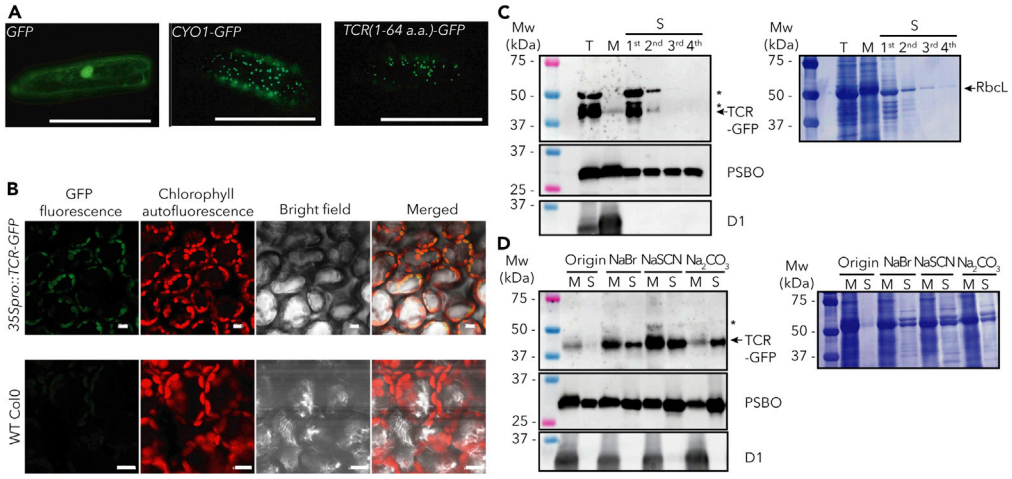

Figure 4. Subcellular localization of TCR

(A) GFP fluorescence in onion epidermal cells transiently expressing *GFP*, *CYO1-GFP*, and *TCR(1–64 a.a.)-GFP*. Scale bars, 30 μm.

(B) GFP and chlorophyll fluorescence from transgenic *A. thaliana* expressing *35Spro::TCR-GFP*. WT (Col 0) was used as a negative control. Scale bars, 10 μm.

(C) Western blotting using anti-GFP, anti-PSBO, and anti-D1 antibodies. T, total chloroplast; M, thylakoid membrane fraction after four washes with 10 mM Na-pyrophosphate-NaOH, pH 7.8; S, soluble-protein fractions (collected in the supernatant at every washing step [first, second, third, and fourth]).

(D) The thylakoid membrane fraction shown in (C) was used as the original fraction (Origin), which was treated with different salts and applied to western blotting. Subsequently, the PVDF membranes were stained with Coomassie blue (right). RbcL, Rubisco large subunit.

Green tissue-specific expression of *TCR*

To investigate the location and timing of *TCR* expression in *A. thaliana*, we performed a histochemical analysis using a *TCR* promoter-fused *GUS* expression construct. The putative promoter region (2,000 bp upstream of the start codon) of *TCR* drove *GUS* expression at very early stages of plant development. Specifically, intensive GUS activity was observed in cotyledons, mature leaves, and hypocotyls at the seedling stage (from day 1–3; Figures 5A and 5B). These high GUS activity patterns were observed over 17 days on MS agar plates (Figures 5A–5E). GUS expression was observed at the tips of emerging leaves (Figures 5C and 5E). Notably, the GUS expression patterns were not uniform (Figure 5C), as higher activity was detected in mesophyll cells near stomata and veins of the leaves of 5-day-old cotyledon (Figure 5G). The 17-day-old transgenic plants were transferred to soil and further grown until flowering and producing fruits. In reproductive tissues, *GUS* expression was observed only in green regions, such as sepals, green seeds, and fruit coats (29-day-old plant; Figure 5F), indicating that the *TCR* promoter is active during seed development after pollen fertilization. Moreover, the wounding of transgenic plants led to the observation of *GUS* expression specifically at the damaged areas, especially in the mesophyll cells and root hairs that surrounded the wounded areas (Figure S3). These data indicate that *TCR* is expressed mainly in green tissues at very early stages of plant growth and at the seed-development stage, and that wounding induced the local expression of *TCR*, even in the roots.

We found that the putative TCR promoter contained binding sites of many transcription factors, such as Dof2, Dof3, HMG-1, MNB1A, PBF, ARR10, SOC1, SEP3, and MYC3, as revealed through the CircadiaNET web server (http://viridiplantae.ibvf.csic.es/circadiaNet/). MYC3, a member of basic-helix-loop-helix (bHLH) transcription factor family, regulates genes involved in tryptophan, jasmonic acid, and other stress responses (Cheng et al., 2011; Fernández-Calvo et al., 2011; Schweizer et al., 2013; Smolen et al., 2002). SOC1 and SEP3 regulate genes involved in the flowering time control (Lee et al., 2008; Liu et al., 2008) and floral organogenesis (Honma and Goto, 2001; Pelaz et al., 2000). These results suggested that TCR expression is controlled by different environmental changes through several transcription factors.

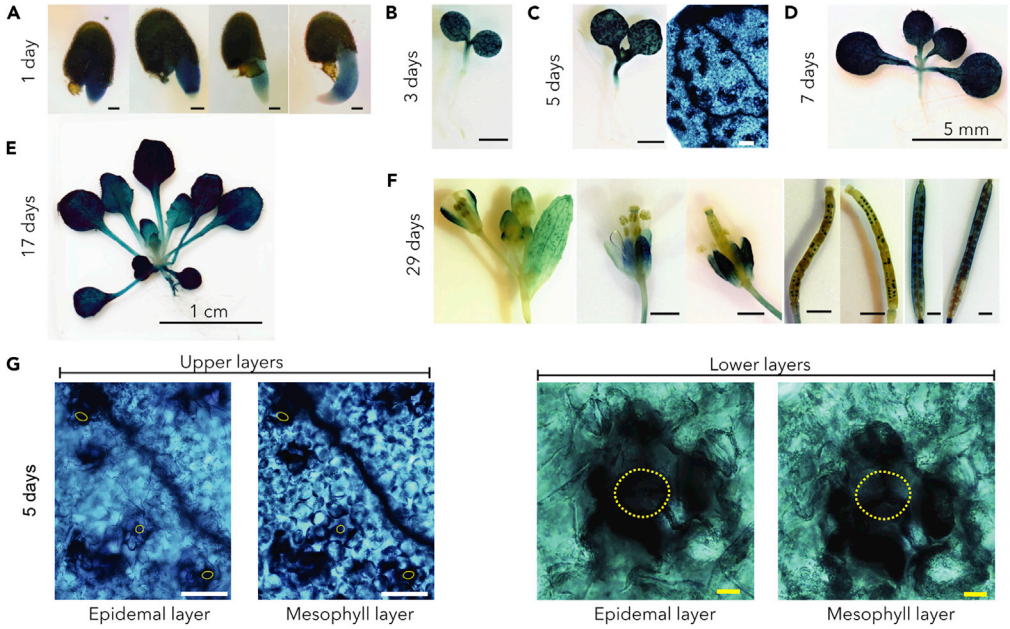

Figure 5. Histochemical analysis of *TCR*-promoter-*GUS* expression

(A) Germinating seeds after 1-day illumination.

(B) 2-day seedling.

(C) 5-day seedling.

(D) 7-day seedling.

(E) 17-day seedling.

(F) Flowers and fruits from a 29-day transgenic plant.

(G) Leaf tissue of 5-day cotyledons. The yellow circles indicate the stomatal position on epidermal layers. Observations were focused on the epidermal layer, to determine the position of stomata; subsequently, the focus shifted to the mesophyll layer, to the detect mesophyll cells that surrounded stomata, which showed strong GUS expression. Scale bars, 0.1 mm (1 day), 1 mm (3, 5, and 29 days), and 100 μm in (G) (white) and 10 μm in (G) (yellow).

See also Figure S3.

tcr mutant is sensitive to light stress conditions

Because T-DNA insertional knockout lines of *TCR* are not available, we knocked out *TCR* using the CRISPR/Cas9 system. The diagram provided in Figure S4A depicts the experimental process. We isolated one frameshift mutant that carried a large deletion (83 amino acid) and replacement (23 amino acid) in the *TCR*-coding region (Figure S4B). The frameshift mutant caused 52% loss of amino acid residues of TCR peptide with the remaining C-terminal (without counting the predicted chloroplast transit peptide) containing only 21 alternative amino acid residues, suggesting that TCR is completely knocked out in the *tcr* mutant. After backcrossing with wild-type (WT), a homozygous line was used as a knockout mutant of *tcr*.

No significant phenotypic differences were observed between WT and *tcr* plants regarding growth (Figure 6A), pigment content (Figure 6B), chloroplast ultrastructure (Figure 6C), and protein levels of some photosynthetic complexes (Figure 6D and 6E). The protein levels of other photosynthetic complexes were also checked by mass-spectrometry-based quantitation. The mass spectrometric data show that there are no differences in the photosynthetic complexes in WT and *tcr* lines (Table S1).

To obtain additional insights into the physiological importance of the TCR, the photosynthetic activities of *tcr* plants were analyzed under different light stress conditions. We first characterized the high-light sensitivity of the *tcr* mutant. Detached leaves were exposed to intense light (1,500 μmol photons m^{-2} s^{-1}) for 8 h, and PSII photoinhibition was analyzed. A more pronounced photoinhibition was observed in *tcr* versus WT plants, and the maximum quantum yield of PSII (F_v/F_m) was lower in *tcr* versus WT plants (Figure 6F). This phenotype was complemented partly in a complementing line Compl-1 and was complemented fully in another complementing line Compl-2 (Figure 6F). Notably, real-time PCR analysis with mRNA isolated

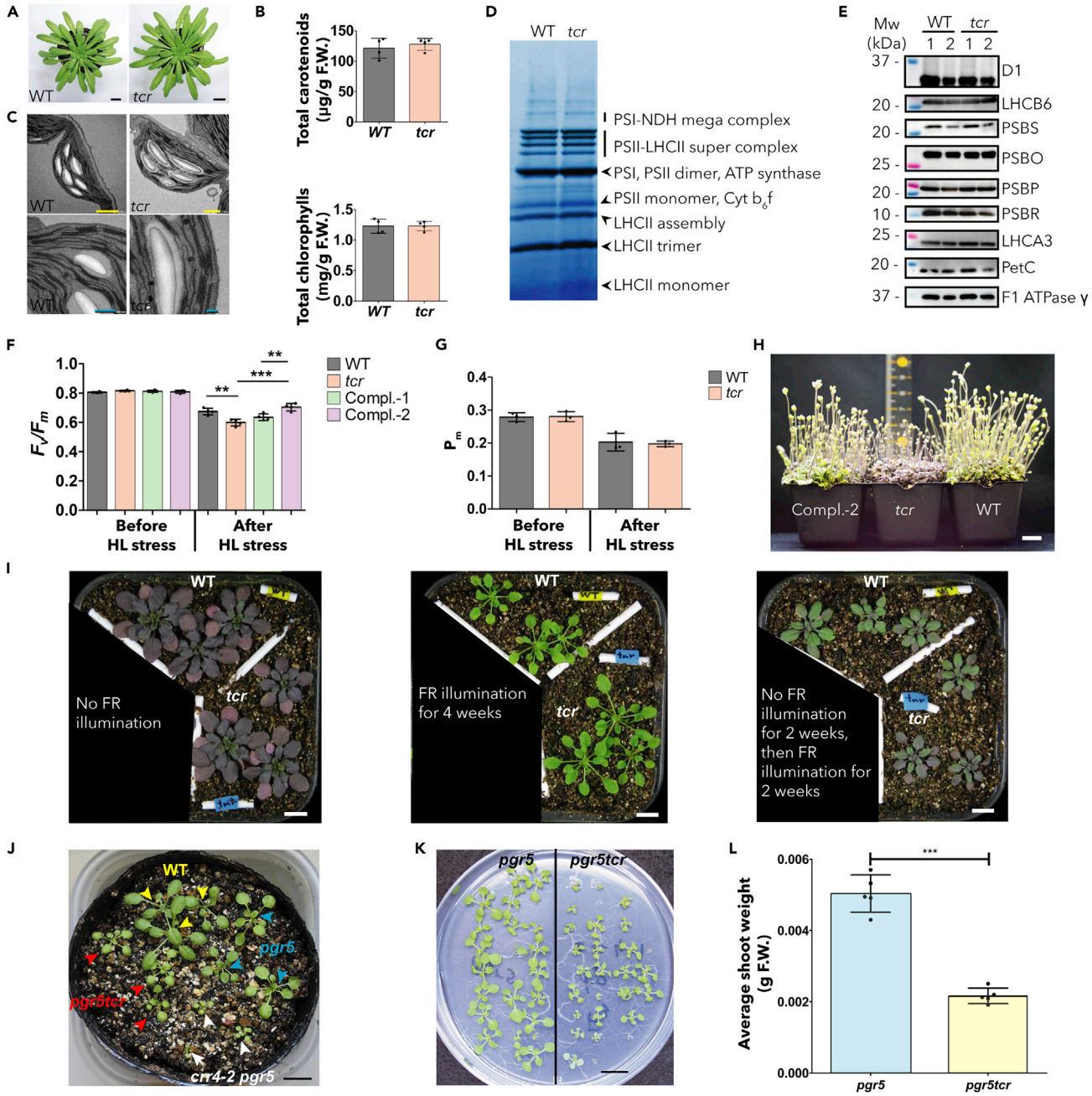

Figure 6. Characterization of the phenotype of the *tcr* mutant

(A) Shoot phenotype of plants grown under short-day conditions for 70 days. Scale bars, 1 cm.

(B) Pigment content of the plants shown in (A).

(C) Ultrastructure of chloroplasts, as observed using transmission electron microscopy. Leaf samples were collected from 19-day-old plants. Yellow scale bars, 2 µm (WT) and 1 µm (*tcr*); blue scale bars, 500 nm (WT) and 200 nm (*tcr*).

(D) Analysis of photosynthetic protein complexes via large-pore Blue Native PAGE.

(E) Western blotting using specific antibodies. Loading: 1, 3.1 µg/well; 2, 1.55 µg/well.

(F) Maximum quantum yield at PSII before and after 8 h of high-light stress. Detached leaves from 50-day-old plants were used. All plants were grown under short-day conditions. Data are the mean ± SD (n = 4). Statistically significant differences were analyzed as shown in the figure for the different types of plants using the two-tailed Student's t test with a 95% confidence interval (**$p < 0.01$, ***$p < 0.001$).

(G) Maximum P700 oxidation at PSI before and after 8 h of high-light stress. Detached leaves from 50-day-old plants were used. All plants were grown under short-day conditions. Data are the mean ± SD (n = 4).

(H) Plants were grown under continuous strong light (1,200 µmol photons m^{-2} s^{-1}) from germination until reproduction (flowering). Scale bar, 1 cm.

Figure 6. *Continued*

(I) Phenotypic observation of plants grown under fluctuating light conditions for 4 weeks with or without FR illumination (λ_{max} = 740 nm). The fluctuating light (FL) cycle was high light (HL, 700 μmol photons m^{-2} s^{-1}, red + blue LEDs) for 2 min, followed by low light (LL, 30 μmol photons m^{-2} s^{-1}, fluorescent lamps) for an additional 2 min. Plants were treated with FL during the light phase of the 8 h/16 h light/dark cycle. Far red (FR) light was induced with an intensity of 50 μmol photons m^{-2} s^{-1} during the HL phase and an intensity of 10 μmol photons m^{-2} s^{-1} during the LL phase of FL. FR source: IR LED Stick (NAMOTO). Scale bar, 1 cm.

(J) Shoot phenotype of WT, *pgr5*, *crr4-2pgr5*, and *pgr5tcr* plants. Scale bar, 1 cm.

(K) Shoot phenotypes of *pgr5* and *pgr5tcr* plants. Plants were grown under short-day conditions for 19 days on 1/2 MS agar. Scale bar, 1 cm.

(L) The mean shoot mass of *pgr5* and *pgr5tcr* plants grown under the conditions indicated for (K). Data are the mean ± SD (n = 5, 10–16 plants per measurement). Statistically significant differences were analyzed as shown in the figure for the different types of plants using the two-tailed Student's t test with a 95% confidence interval (***$p < 0.001$). F.W., fresh weight.

See also Figure S5.

from whole shoot tissues indicated that *TCR* mRNA levels in Compl-1 and Compl-2 were similar to and higher than those in WT, respectively (Figure S4C). Given that the *TCR* expression in leaves is not uniform (Figure 5C), TCR expression in Compl-1, driven by the constitutive 35S promoter, may be lower than that in WT at specific areas, which may be a reason why Compl-1 could not fully complement the *tcr* phenotype. After the high-light treatment, no significant change in P_m values was observed in *tcr* compared with WT plants (Figure 6G), suggesting that the *tcr* mutation does not cause photoinhibition at PSI upon the high-light treatment. We also grew plants under high-light conditions (1,200 μmol photons m^{-2} s^{-1}) from germination to the reproductive stage. As shown in Figure 6H, all plants accumulated anthocyanins during the vegetative growth stage; however, when the plants grew to the reproductive stage, plant growth of *tcr* lines was reduced relative to WT and Compl-2 plants, indicating the importance of TCR function for the high-light stress response.

Because fluctuating light potentially induces PSI photoinhibition because of the over-reduction of P700 (Shimakawa and Miyake, 2018b), next we checked the phenotype of *tcr* and WT plants under long-term (4 weeks) fluctuating-light treatment. In this condition, both WT and *tcr* leaves accumulated a large amount of anthocyanin (Figure 6I, left), suggesting a strong ROS accumulation caused by the over-reduction of P700 (Xu et al., 2017; reviewed by Li et al., 2009). However, continuous far-red (FR) light (λ_{max} = 740 nm) illumination, which specifically oxidizes P700 (Kono et al., 2017), during the fluctuating-light treatment rescued the phenotype of the photo-oxidative stress in both WT and *tcr* plants, and anthocyanin did not accumulate in leaves (Figure 6I, middle), indicating the importance of FR light for the reduction of ROS generation and PSI photoinhibition (Kono et al., 2017), and, consequently, PSII photoprotection. Interestingly, when plants were grown under fluctuating light without FR for 2 weeks, followed by FR illumination for an additional 2 weeks, *tcr* leaves accumulated higher anthocyanin than did WT leaves (Figure 6I, right). It is possible that FR illumination during the last 2 weeks of the treatment rescued PSI from photoinhibition to a greater extent in WT versus *tcr* plants, suggesting the importance of TCR for P700 oxidation and PSI photoprotection.

To further characterize the *tcr* mutant, we crossed the *pgr5* and *tcr* lines to produce the *pgr5tcr* double mutant and proceeded to characterize its phenotype under ambient air. Under short-day conditions, the *pgr5tcr* double mutant showed delayed growth on soil (Figures 6J and S5A) and MS agar medium (Figure 6K) compared with *pgr5* plants; the average shoot weight of *pgr5tcr* was ~50% that of the *pgr5* line under short-day (Figures 6L and S5B) and long-day (Figures S5C and S5D) conditions. Also, growth retardation could be observed in *crr4-2pgr5* double mutants, which is stronger than those observed in *pgr5tcr* double mutants (Figure 6J). Notably, *crr4-2pgr5* was reported as a typical mutant in which both NDH-CET and PGR-CET are inhibited due to the lack of NDH-complex and PGR5 protein (Munekage et al., 2004; Yamamoto et al., 2011).

tcr mutation affects the redox states of the PQ pool

Next, we investigated the effects of the *tcr* mutation on the redox states of the PQ pool. When actinic-light illumination was turned off, chlorophyll fluorescence was transiently increased in the dark (Figures 7A and 7B). This phenomenon, called the post-illumination chlorophyll fluorescence transient (PIFT), is caused by the reduction of the PQ pool by the Fd-dependent CET from PSI (Gotoh et al., 2010). In fact, the specific excitation of the PSI by FR illumination resulted in a decrease in the fluorescence (Figures 7A and 7B), which supported the notion presented above. Although no significant PIFT changes were detected between WT and *tcr* plants (Figures 7A and 7B), we observed a significant decrease in the PIFT signal in *pgr5tcr*

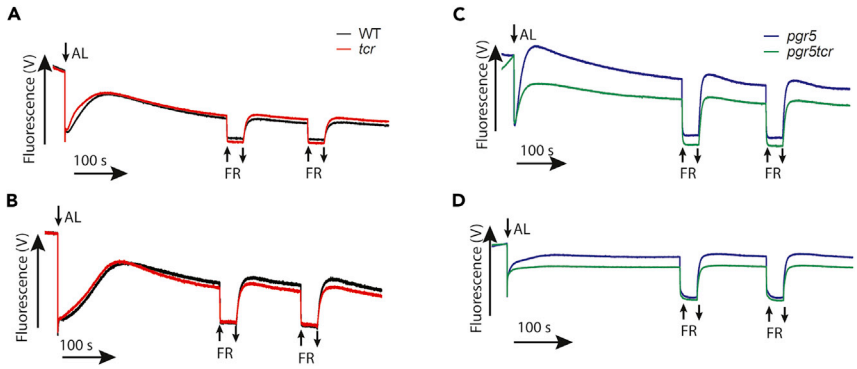

Figure 7. Post-illumination chlorophyll fluorescence transient (PIFT) analysis of WT and mutant plants

(A–D) PIFT analysis of WT and mutant plants after AL pre-illumination for 2 min (A and C) or 5 min (B and D). The fluorescence was normalized to the point at which AL was turned to OFF. ↑, Light ON; ↓, light OFF; ML, measuring light; AL, red actinic light; FR, far-red light; ST, saturating pulse. All plants were grown under short-day conditions for 49–56 days on soil.

See also Figure S6.

compared with *pgr5* specimens when plants were shifted to the dark after 2 and 5 min of actinic-light illumination (Figures 7C and 7D, respectively). Additionally, full trace of the chlorophyll fluorescence (Figure S6) showed that the second rise of fluorescence after actinic light was turned on in *pgr5tcr* occurred faster than in *pgr5*, indicating that the PQ pool in *pgr5tcr* was reduced faster than in *pgr5*. These results implied that TCR accepted electrons from PSI, and the *tcr* mutant decreased the stromal electron sink during illumination. Consequently, TCR contributed to PQ pool(s) oxidation and reduction at least under post-illumination conditions, the importance of which is increased when the PGR5-dependent CET and/or LET are impaired.

Effect of the *tcr* mutation on P700 oxidation

To investigate further the possibility that TCR is involved in electron flows from PSI, next we characterized the P700 oxidation/reduction kinetics upon actinic-light illumination. As expected, the relaxation of Y(NA) and induction of Y(ND) were delayed in *tcr* with WT plants at the induction stage (<2 min) upon turning on the actinic light (Figures 8A and 8B), indicating that electron acceptance from PSI is limited and that the oxidation of P700 is lowered in the *tcr* line. In steady-state conditions of actinic-light illumination (>2 min), Y(I) was slightly lower in *tcr* than it was in WT plants (Figure 8C), indicating that the electron flow from PSI to Fd and/or PC to PSI is limited in *tcr* specimens, which results in lowered PSI activity. Notably, the *tcr* phenotypes were partially and fully complemented in the complement lines Compl-1 (Figure S7) and Compl-2 (Figures 8D, 8E, and 8F), respectively.

We also investigated the induction kinetics of P700 oxidation upon FR light illumination using a Joliot-type spectrophotometer. We characterized the P700 oxidation/reduction kinetics of WT and *tcr* plants that were pre-treated with two distinct light conditions; one was used to monitor specifically LET in which electron transfer from PSI to $NADP^+$ would be dominant (plants were pre-illuminated with red light for 10 min before measurements), whereas the other treatment was used to monitor CET in which electrons from PSI to Cyt b_6f would be dominant (plants were kept in dark for 10 min, followed by irradiation with a saturating pulse for 100 ms before measurements) (Ghysels et al., 2013; Joliot and Joliot, 2006; Talts et al., 2007). When plants were pre-treated to monitor LET, the WT and *tcr* lines showed FR-induced P700 oxidation without any intermediates (Figure 8G); in contrast, when WT plants were pre-treated to monitor CET, two-step oxidation of P700 was observed, i.e., FR illumination resulted in rapid P700 oxidation, followed by re-reduction of P700 2 s after the FR illumination and re-oxidization of P700, as reported previously (Figure 8H, black line) (Ghysels et al., 2013; Nagarajan et al., 2014; Talts et al., 2007). Conversely, we observed an abnormal three-step P700 oxidation in *tcr* when the CET was dominant; a small shoulder was additionally observed at 5 s after turning on the FR illumination (Figure 8H, red line; asterisk). This suggests that TCR function is related to the P700 oxidation process, especially when the CET is dominant, although the exact reason for the abnormal three-step P700 oxidation kinetics observed in *tcr* plants is unknown.

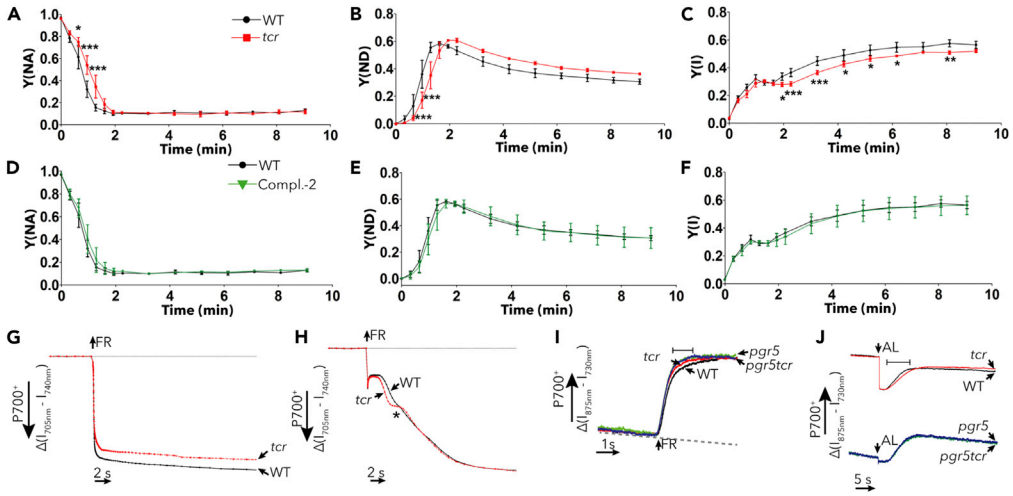

Figure 8. PSI activities and oxidation/reduction kinetics of P700

(A and D) Measurement of the acceptor side limitation at PSI. *p < 0.05, ***p < 0.001 (one-way ANOVA followed by Tukey's test with a 95% CI). Plants were grown on soil under short-day conditions for 56 days. AL = 150 μmol photons m^{-2} s^{-1}, P700 ML = 10, RT = 20°C. Dark adaptation time = 30 min. Data represent the mean ± SD (n = 3).

(B and E) Measurement of the donor side limitation at PSI. ***p < 0.001 (one-way ANOVA followed by Tukey's test with a 95% CI). Plants were grown on soil under short-day conditions for 56 days. AL = 150 μmol photons m^{-2} s^{-1}, P700 ML = 10, RT = 20°C. Dark adaptation time = 30 min. Data represent the mean ± SD (n = 3).

(C and F) Measurement of the PSI quantum yield. *p < 0.05, **p < 0.01, ***p < 0.001 (one-way ANOVA followed by Tukey's test with a 95% CI). Plants were grown on soil under short-day conditions for 56 days. AL = 150 μmol photons m^{-2} s^{-1}, P700 ML = 10, RT = 20°C. Dark adaptation time = 30 min. Data represent the mean ± SD (n = 3).

(G and H) Measurement of P700 in the presence of a dominant LET or a dominant CET, respectively, using a Joliot-type spectrometer. The asterisk indicates an unusual signal that was not observed in WT plants. ↑, Light ON; ↓, light OFF; FR, far-red light. All plants were grown on soil under short-day conditions for 49–56 days.

(I and J) Measurement of P700 after the adaptation of plants to the dark and light, respectively, using a DUAL-PAM-100 system. The FR was kept ON during the measurement as shown in the panel (L). The P700 signals in (K) were double-normalized using the lowest (P_o) and the highest (P'_m) values. Dashed line, P_o. The P700 signals of WT and *tcr* or *pgr5* and *pgr5tcr* plants in (L) could not be double-normalized using the point at which AL was turned to OFF or to the lowest value of P700. Bars, regions showing differences between WT and mutant plants. ↑, Light ON; ↓, light OFF; AL, red actinic light; FR, far-red light. Plants were grown on soil under short-day conditions for 49–56 days.

See also Figure S7.

We also monitored the oxidation kinetics of P700 at a relatively faster range using the DUAL-PAM-100 system. When dark-adapted plants were illuminated with FR light, the P700 oxidation kinetics in *tcr*, *pgr5*, and *pgr5tcr* plants was faster than that detected in the WT counterparts (Figure 8I, red, green, and blue lines, respectively; marked bar), suggesting that the stromal electron sink in the dark is smaller in the mutants versus WT plants, as reported previously for the *pgr5* mutant (Okegawa et al., 2007). We also monitored the P700 reduction/oxidation kinetics upon turning off the actinic light under FR-light illumination. Upon turning off the actinic light, sudden P700 reduction was observed in WT and *tcr* plants, which was significantly diminished in *pgr5* and *pgr5tcr* plants (Figure 8J). This implies that, in *pgr5* background, P700 is already highly reduced compared with the WT background under actinic-light illumination conditions, because of the inhibition of PGR5-dependent CET and/or LET. Two seconds after turning off the actinic light, P700 was gradually re-oxidized by FR light in WT plants (Figure 8J; marked bar), which was slowed down in *tcr* lines, suggesting that P700 oxidation is reduced in the latter via limited electron acceptance from PSI. The decreased P700 oxidation kinetics observed upon *tcr* mutation was not observed in the *pgr5* background (Figure 8J). Taken together, these results suggest that TCR plays a role in the maintenance of the P700 oxidation/reduction status, which seems to be important when the stromal electron sink is limited.

We next tested $P700^+$ reduction kinetics by the PC-dependent electron transfer. Specifically, leaves were illuminated by FR light for 30 s, and then $P700^+$ was completely oxidized to the greatest level (Pm) by supplying saturating light for 3 ms. After turning off the saturating light, $P700^+$ signal was decreased, which reflected the $P700^+$ reduction by PC (Figure S8). No difference was observed between the recorded

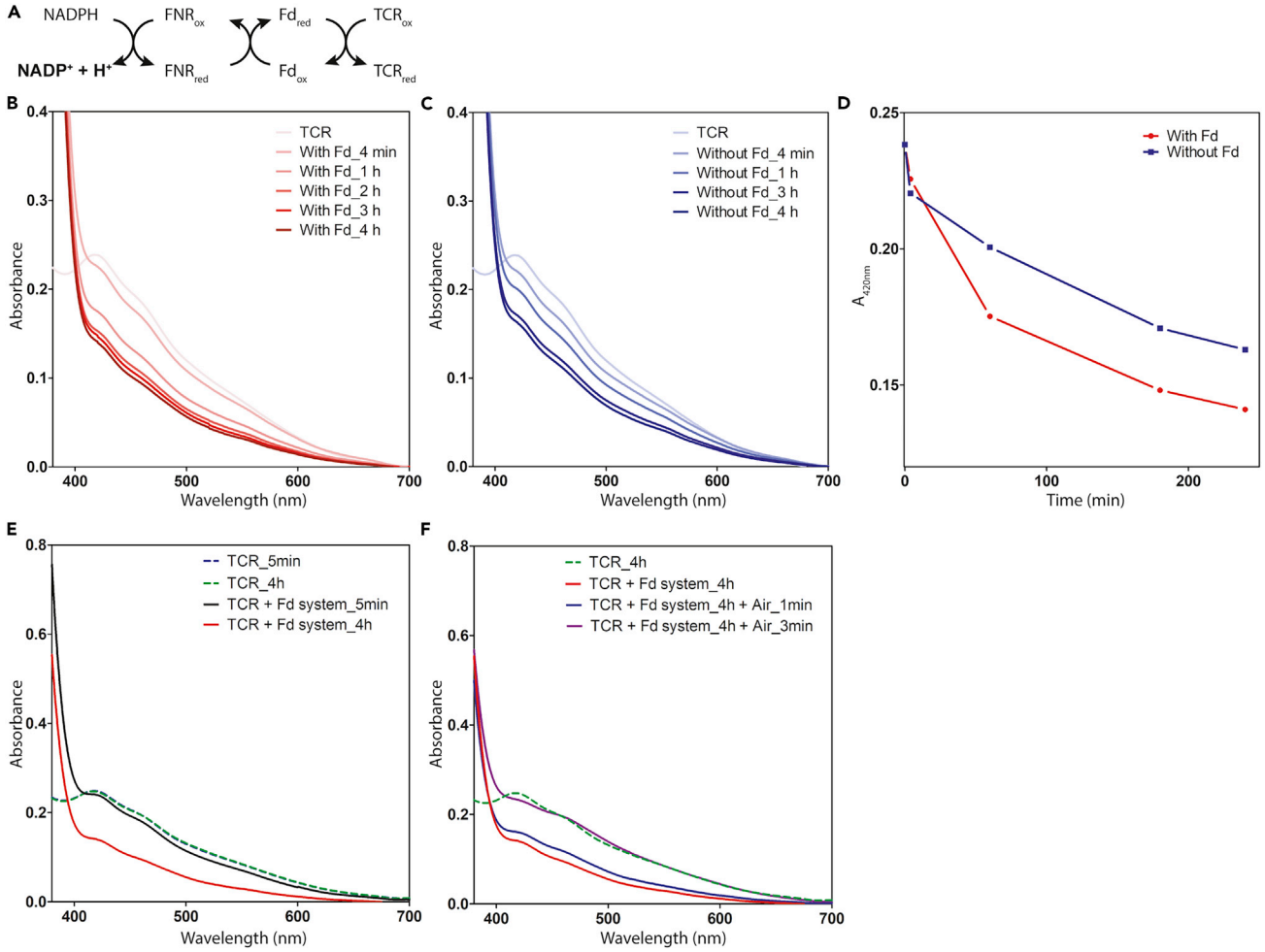

Figure 9. Fd-dependent reduction of TCR

(A) Schematic representation of the experiment performed to reduce TCR by NADPH, FNR, and Fd *in vitro*.

(B) Time-lapse observation of the reduction of TCR *in vitro* by NADPH, FNR, and Fd.

(C) Time-lapse observation of the reduction of TCR *in vitro* by NADPH and FNR.

(D) Time dependency of absorbance change at 420 nm (A_{420nm}) due to the reduction of iron-sulfur center in TCR in (B) and (C).

(E) Absorption change in the purified TCR 5 min and 4 h after the addition of buffer only (dashed lines) or NADPH, FNR, and Fd (solid lines, + Fd system) under anaerobic conditions.

(F) Absorption change of the reduced TCR (by the Fd system) after exposure to ambient air for 1 and 3 min

$P700^+$ kinetics of *tcr*, Compl-2, and WT plants (Figures S8A and S8B), indicating that electron transfer from Cyt b_6f to the PSI donor side is normal in *tcr* mutant. This further suggests that alteration of P700 oxidation/reduction status caused by the *tcr* mutation (Figures 8I and 8J) may result from limitation of the electron flow downstream of the acceptor side of PSI.

Given Fd is the primary electron acceptor of PSI, TCR may receive electrons from Fd. To test this possibility, we performed *in vitro* reduction of TCR by Fd (Figure 9). In the presence of a large amount of NADPH, electrons were transferred to FNR and Fd, which then potentially reduce TCR (Figure 9A). It is noteworthy that, in the reaction mixture, the concentration of Fd and FNR was ~400-fold lower than that of TCR. Upon addition of a large amount of NADPH (1 mM), decrease in A_{420} was observed (Figure 9B), indicating the electron transfer from NADPH to TCR via FNR and Fd. TCR reduction could be observed even without Fd (Figure 9C), although the TCR reduction rate without Fd was slower than that observed with Fd (Figure 9D). We confirmed that the TCR reduction was not observed without the Fd system for 4 h (Figure 9E, dashed lines). These results indicated that Fd catalyzes TCR reduction. In turn, A_{420} was increased 1 min after exposure to

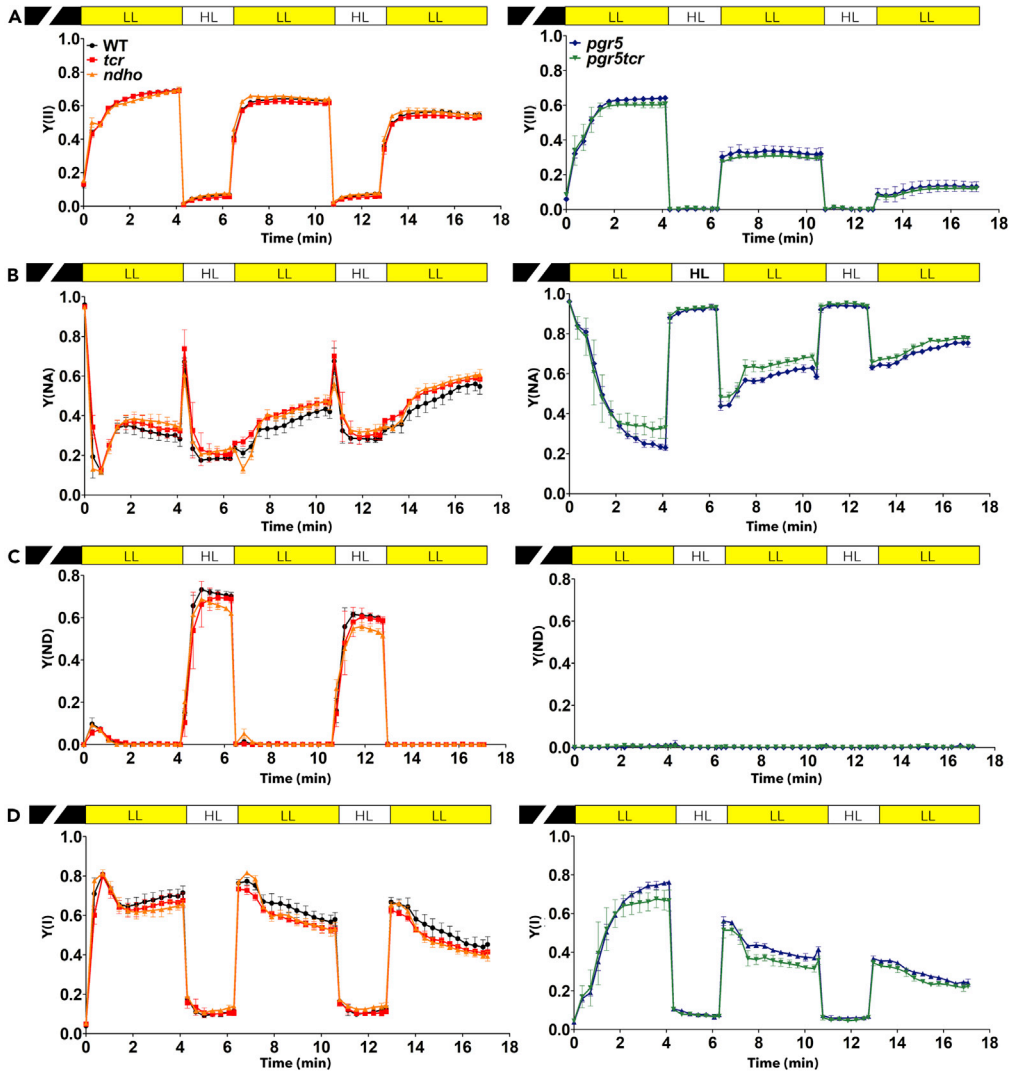

Figure 10. Photosynthetic activity under fluctuating light conditions

(A) PSII quantum yield.

(B) Electron limitation at the acceptor side of PSI.

(C) Electron limitation at the donor side of PSI.

(D) PSI quantum yield. Plants were grown on soil under short-day conditions for 50–57 days. Data represent the mean ± SD (n = 3). LL, 33 μmol photons m^{-2} s^{-1}; HL, 920 μmol photons m^{-2} s^{-1}; dark acclimation time = 30 min; RT = 20°C.

the ambient air of the reaction solution that had been incubated with NADPH for 4 h (Figure 9F, solid blue line) and was fully recovered after 3 min of exposure (Figure 9F, solid purple line). These observations confirmed that the decreased A_{420} reflected TCR reduction. These data demonstrated that TCR is redox active *in vitro*.

To assess further the possibility that TCR is involved in the Fd-dependent electron transfer from PSI, we performed an *in vitro* Fd-dependent PQ pool reduction assay (Munekage et al., 2002; Okegawa et al., 2008). In the absence of antimycin A (AA), thylakoid membranes isolated from WT, *tcr*, and NDH-complex-mutant *crr4-2* lines showed fluorescent increments upon Fd addition, indicating the presence of proper Fd-dependent PQ reduction in the dark (Figure S9). In the presence of AA, although chlorophyll fluorescence was inhibited in all samples, the WT and *tcr* lines exhibited a similar fluorescence increment, and only the *crr4-2* line showed significant fluorescence impairment (Figure S9). This suggests that TCR is not involved in the main CET flows, although this experiment was recently questioned in that the

fluorescent increment may not reflect Fd-dependent PQ reduction (see Discussion for more details) (Fisher and Kramer, 2014).

tcr shares similar photosynthetic parameters with *ndho* under fluctuating light

We next monitored the photosynthetic activities of PSI and PSII under fluctuating-light conditions in WT, *tcr*, *pgr5*, *pgr5tcr*, and NDH-complex null-mutant *ndho* plants. All mutants exhibited altered PSI activity compared with the WT (Figure 10). Specifically, the *tcr* mutant showed higher Y(NA) than did WT plants from the second-round shift from high light to low light (Figure 10B). This phenotype was also observed (even more significantly) in *pgr5tcr* versus *pgr5* plants upon the shift from high light to low light (Figure 10B). Moreover, slight changes in Y(ND) levels were observed in *tcr* compared with WT plants, especially when the light intensity was changed from low light to high light (Figure 10C). An increase in Y(NA) accompanied the decrease in PSI quantum yield, Y(I), in *tcr* compared with WT (Figure 10D). The *ndho* mutant exhibited similar phenotypes to those observed in the *tcr* mutant under fluctuating light conditions, suggesting that the physiological function and impact of the TCR-dependent electron transfer are similar to those of NDH-CET. Notably, the *ndho* phenotypes were similar to those reported previously (Nikkanen et al., 2018; Shimakawa and Miyake, 2018b; Suorsa et al., 2012).

DISCUSSION

TCR is a plastidial iron-sulfur protein

TCR is a low-copy gene specifically found in oxygenic phototrophs and its expression level is strictly controlled in *A. thaliana* (Dunand et al., 2011), suggesting its importance for photosynthesis regulation. Similar to that reported for PSBO, TCR-GFP was detected in both thylakoid membranes and soluble fractions (Figures 4C and 4D), suggesting that TCR functionally interacts with thylakoid-membrane-anchored protein(s), although its exact target(s) remain unclear. We determined that TCR contained an iron-sulfur cluster based on the observation that it exhibited absorption at around 420 nm (Figure 2C), with an ESR signal at g = 2.028 (Figure 3A), both of which are typical features of 3Fe–4S cluster proteins (Hoppe et al., 2011; Lippard and Berg, 1994; Nakamaru-Ogiso et al., 2002). Furthermore, TCR may contain a redox-active disulfide bond (Figure S2B), and its reduction induced alterations in the redox potential and/or structure of the protein (Figures 2D and 2E). These results established that TCR is a plastidial iron-sulfur protein involved in photosynthetic electron transfer.

TCR expression patterns, as examined by the promoter-*GUS* fusion analysis (Figure 5), were similar to those of other photosynthetic regulatory genes, such as *Pisum sativum* thioredoxin *f*1 (*PsTRXf1*), thioredoxin *m*1 (*PsTRXm1*), cucumber *VDE* (*CsVDE*), and *A. thaliana PGR5* (*AtPGR5*) (Barajas-López et al., 2007; Li et al, 2013, 2015; Long et al., 2008). Specifically, all these genes are highly expressed in cotyledons, mature leaves, and other green tissues, supporting the hypothesis that TCR is involved in photosynthetic control. Furthermore, as shown for *TCR* (Figures 5 and S3), *AtPGR5* (Long et al., 2008) and *CsVDE* (Li et al., 2015) expression patterns were variable, and *PsTRXf1*, *PsTRXm1*, *CsVDE*, and *AtPGR5* were expressed in non-photosynthetic organs, such as flower sepals (*PsTRXf1*, *PsTRXm1*, *CsVDE*, and *AtPGR5*), green seeds (*PsTRXm1*), fruit coats (*CsVDE*, *PsTRXf1*, and *PsTRXm1*), hypocotyls (*CsVDE*, *PsTRXf1*, and *AtPGR5*), vasculatures, and stems (*CsVDE* and *AtPGR5*) (Barajas-López et al., 2007; Li et al, 2013, 2015; Long et al., 2008). Interestingly, *AtPGR5* expression was induced upon wounding (Long et al., 2008), similar to TCR (Figure S3). Aside from the photosynthetic control discussed in this study, these results suggested TCR's additional functions related to germination, plant reproduction, and abiotic stress responses, as discussed previously for TRX*f*, TRX*m* (Barajas-López et al., 2007), VDE (Li et al., 2015), and PGR5 (Long et al., 2008).

TCR controls electron transfer around PSI

TCR is redox active *in vitro* (Figure 9), and mutational loss of *TCR* affected the P700 oxidation kinetics (Figure 8) as well as the redox status of PQ pools (Figure 7), suggesting that TCR controls the electron transfer around the PSI acceptor side for P700 oxidation. Because the purified TCR was oxidized upon exposure to ambient air *in vitro* (Figure 2C), and had a relatively low redox potential (Figures 2C and 3A), TCR may also contribute to the water-water cycle by reducing oxygen with electrons derived from Fd/PSI.

CO_2 assimilation is limited when the CBB cycle cannot be fully activated. This is observed in nature when plants suffer drought-stress-induced stomatal closure, cold-stress-induced metabolic changes, high-light-stress-induced photorespiration, and nutrient deprivation (reviewed by Demmig-Adams and Adams, 1992; Asada, 1999). Short-term limitation of CO_2 assimilation is observed when dark-adapted plants are exposed to light (Ptushenko et al., 2019). When CO_2 assimilation is low, CET and other alternative electron transfer systems are enhanced, to transfer electrons from PSI to the PQ pool and/or from PSI to O_2 through photorespiration and the water-water cycle. In fact, when plants had just shifted from dark to light conditions, we observed significant differences between WT and *tcr* plants at photosynthetic parameters Y(I), Y(NA), Y(ND) (Figures 8A, 8B, and 8C), and $P700^+$ (Figures 8H and 8J). Also, *tcr* mutant showed clear phenotypes only when plants were treated with high-light and/or fluctuating-light stresses (Figures 6F, 6H, and 6I). As mentioned above, under such conditions, CO_2 assimilation was inhibited. Therefore, we propose that TCR function is especially required when CO_2 assimilation is limited and photorespiration is not fully activated, which supports P700 oxidation to avoid PSI photoinhibition, as the excess electrons accumulated in PSI lead to ROS generation (Tiwari et al., 2016; reviewed by Shimakawa and Miyake, 2018b; Sonoike, 2011). In fact, because the P700 oxidation system receives contributions from various mechanisms (reviewed by Sonoike, 2011; Shimakawa and Miyake, 2018b), PSI photoinhibition is rarely observed, even under natural strong-light illumination (2,000–3,000 μmol photons m^{-2} s^{-1}) (Shimakawa and Miyake, 2018b); hence, PSI photoinhibition in *tcr* was not different from that in WT under strong-light conditions (1,500 μmol photons m^{-2} s^{-1}, Figure 6G).

TCR-dependent electron transfer affects CET activity

We observed many similarities between the *tcr* and NDH-CET mutants (*ndho*, *crr2-1*, and/or *crr4-2*). First, neither *tcr* nor *ndho* plants exhibited any visible phenotype under controlled conditions (Figures 6A–6C) (Suorsa et al., 2012). Second, most of the photosynthetic parameters for PSII and PSI activities were similar between *tcr* and *ndho* plants (Figure 10). Third, both the *pgr5tcr* and *crr4-2pgr5* mutants showed growth retardation compared with the *pgr5* mutant (Figures 6J–6L and S5) (Munekage et al., 2004; Yamamoto et al., 2011). Fourth, high-light treatment on either *tcr* or NDH-CET mutants could cause PSII photoinhibition (Figure 6F) (Endo et al., 1999). Finally, the expression profiles of *TCR* and NDH-complex genes, such as *PnsL2*, *PnsL3*, *CRR7*, *NdhN*, and *NdhL*, were similar (Figure 1A) (Aoki et al., 2016; Szklarczyk et al., 2015). These observations suggest that TCR-dependent electron transfer affects CET in *A. thaliana*. In fact, the PIFT signal, which was abolished in NDH mutants (Kamruzzaman Munshi et al., 2005; Takabayashi et al., 2009), was normal in the *tcr* mutant (Figures 7A and 7B), suggesting that TCR-dependent electron transfer is independent of NDH-CET.

Based on the structural characterization of photosynthetic protein complexes, an alternative pathway for CET, other than PGR-CET and NDH-CET, has been proposed in which Fd transfers electrons to PQ through a putative protein super-complex embedded in the thylakoid membranes (Johnson, 2011; Nawrocki et al., 2019a, 2019b, 2019c). The putative CET super-complex (FQR complex) may include PSI, Cyt b_6f, FNR, PGRL1, PGR5, ANR1, and CAS; thus the FQR-complex-dependent CET is independent from the NDH-CET, but may partially overlap with the PGR-CET (Nawrocki et al., 2019a, 2019b, 2019c). Although experimental evidence is still lacking, the existence of the FQR complex was supported by the isolation of the Cyt b_6f-PSI super-complex (Steinbeck et al., 2018; Yadav et al., 2017), the Cyt b_6f-FNR complex (Clark et al., 1984; Zhang et al., 2001), and the CAS-ANR1-PGRL1 complex (Terashima et al., 2012), as well as by physical interactions between PGRL1 and PSI, Fd, Cyt b_6f, FNR, and PGR5 (Dal-Corso et al., 2008). In fact, Fd and FNR are encoded by multiple gene copies in the genome, and FNR iso-proteins have various abilities to interact with thylakoid membrane complexes (Goss and Hanke, 2014). Given that Fd and FNR were also involved in LET, and TCR has an affinity with both Fd and FNR to receive electrons (Figures 9B and 9C), TCR may assist to fine-tune electron divergence between the LET and the CET, which are specifically controlled by cell types (e.g., bundle sheath and mesophyll cells) and/or specific physiologic conditions. Given TCR has redox-active cysteine residues (Figures 2D and S2B), oxidation and reduction of the disulfide bond may have a role in the TCR function. Electrons derived from Fd are transferred to the thioredoxin system that affects CBB cycle activation as well as CET (Nikkanen et al., 2018; Okegawa and Motohashi, 2020), suggesting that TCR also functionally interacts with the thioredoxin system, through disulfide-bond exchange, to control electron transfer downstream of PSI.

The isolated thylakoid membranes of *tcr* plants showed a WT-like Fd-dependent fluorescent increment both in the presence and absence of AA (Figure S9), suggesting that TCR is not involved in the Fd-dependent CET. However, this experiment was recently questioned in that it may not reflect CET-dependent PQ reduction; rather, it may reflect Q_A reduction in PSII by Fd *in vitro* (Fisher and Kramer, 2014). Alternatively, it is possible that TCR was inactivated during membrane isolation, because the Fe-S center in TCR is sensitive to oxygen (Figure 2C, mentioned above in the Results section).

TCR appeared after plastid endosymbiosis

According to the endosymbiotic theory, photosynthetic eukaryotes originated from two endosymbiosis events: (1) the endosymbiosis of an ancestor of α-proteobacteria that became mitochondria and (2) the endosymbiosis of an ancestor of cyanobacteria that became plastids (reviewed by Timmis et al., 2004). As TCR homologs exist in most oxygenic phototrophs, including green algae, liverworts, ferns, monocots, and dicots, but not in cyanobacteria (Figure S1), *TCR* might have appeared after the plastid endosymbiosis and after the separation of the green and red lineages, as was the case for the *PGRL1A*, *PGRL1B* (DalCorso et al., 2008), *NPQ4* (reviewed by Niyogi and Truong, 2013), *NPQ1* (Li et al., 2016), and *FdC1* (Guan et al., 2018; Voss et al., 2011) genes. Moreover, the expansion of the content of redox-sensitive cysteines in the proteins of eukaryotes after the first plastid acquisition is believed to coincide with the growing demands of the eukaryotic cells regarding the balancing of the cellular redox states, resulting in protection from oxidative stresses (Woehle et al., 2017). In plants, a large number of cysteine-rich proteins (e.g., thioredoxins, glutaredoxins, peroxiredoxins, and several protein-disulfide isomerases) play essential functions in the hierarchical systems that are used for poising the redox status in stroma and protecting PSI from ROS (Scheibe et al., 2005). Therefore, TCR was established during the evolution of oxygenic phototrophs and contributed to the control of the redox balance in stroma and to the protection of PSI from photodamage.

Limitations of the study

Although this study provides evidences showing that TCR is involved in an alternative electron flow downstream of PSI, further investigation is needed to fully understand the mechanism of the proposed function of TCR. Specifically, this work has not yet fully uncovered the direct electron donor and acceptor of TCR. Furthermore, the stoichiometric ratio between PSI and TCR is still missing due to the lack of the TCR-specific antibody for detecting TCR and the difficulties in identifying the TCR peptide by mass spectrometric analysis.

Resource availability

Lead contact

Further information and requests for resources and reagents should be directed to and will be fulfilled by the Lead Contact, Shinji Masuda (shmasuda@bio.titech.ac.jp).

Materials availability

Materials generated in this study are available from the lead contact with a completed materials transfer agreement.

Data and code availability

Mass-spectroscopy-based proteome data have been deposited to jPOST (https://jpostdb.org) with the accession number JPST000936 or PXD020752.

METHODS

All methods can be found in the accompanying Transparent Methods supplemental file.

SUPPLEMENTAL INFORMATION

Supplemental Information can be found online at https://doi.org/10.1016/j.isci.2021.102059.

ACKNOWLEDGMENTS

The authors thank Professor Kintake Sonoike and Mr. Kazuma Takai (M.Sc.) at Waseda University for device and technical support (Joliot-type spectrometer), Dr. Kentaro Ifuku at Kyoto University for providing

antibodies, Dr. Felix Wolter of KIT-Botanical Institute 2 for his valuable advice about CRISPR/Cas9 system, and Professor Toshiharu Shikanai for *pgr5* and *crr4-2pgr5* mutant seeds. We also thank people in Ohta-Shimojima Laboratory at Tokyo Institute of Technology for device support and the Biomaterial Analysis Division of Tokyo Institute of Technology for technical assistance. This work was partly supported by Nanotechnology Platform Program <Molecule and Material Synthesis> (JPMXP09S20MS1007) of the Ministry of Education, Culture, Sports, Science and Technology (MEXT), Japan, and funded by KAKENHI to H.M. (JP20H05096) and S.M. (19H04719).

AUTHOR CONTRIBUTIONS

M.D.L.T. and S.M. designed the research. M.D.L.T. performed most experiments and wrote the first draft paper. D.M. contributed to launch the research and to perform localization analysis. S.O. contributed to histochemical *GUS* expression analysis. J.N. and T.H. contributed to biochemical analysis of His6-TCR. M.K. performed phenotypic analysis of WT and *tcr* grown under fluctuating light condition. H.M. performed ESR analysis. T.N. and H.T. contributed to mass spectrometric analysis of chloroplast proteins. Y.O. and K.M. performed Fd-dependent chlorophyll fluorescence increment analysis. All authors discussed and interpreted the data.

DECLARATION OF INTERESTS

The authors declare no competing interests.

Received: November 3, 2020
Revised: December 8, 2020
Accepted: January 8, 2021
Published: February 19, 2021

REFERENCES

Ahmad, N., Michoux, F., and Nixon, P.J. (2012). Investigating the production of foreign membrane proteins in tobacco chloroplasts: expression of an algal plastid terminal oxidase. PLoS One *7*, e41722.

Aoki, Y., Okamura, Y., Tadaka, S., Kinoshita, K., and Obayashi, T. (2016). ATTED-II in 2016: a plant coexpression database towards lineage-specific coexpression. Plant Cell Physiol. *57*, e5.

Arnon, D.I., Allen, M.B., and Whatley, F.R. (1954). Photosynthesis by isolated chloroplasts. Nature *174*, 394–396.

Asada, K. (1999). The water-water cycle in chloroplasts: scavenging of active oxygens and dissipation of excess photons. Annu. Rev. Plant Physiol. Plant Mol. Biol. *50*, 601–639.

Bairoch, A., Apweiler, R., Wu, C.H., Barker, W.C., Boeckmann, B., Ferro, S., Gasteiger, E., Huang, H., Lopez, R., Magrane, M., et al. (2005). The universal protein resource (UniProt). Nucleic Acids Res. *33*, 154–159.

Barajas-López, J.D.D., Serrato, A.J., Olmedilla, A., Chueca, A., and Sahrawy, M. (2007). Localization in roots and flowers of pea chloroplastic thioredoxin *f* and thioredoxin *m* proteins reveals new roles in nonphotosynthetic organs. Plant Physiol. *145*, 946–960.

Bennoun, P. (1982). Evidence for a respiratory chain in the chloroplast. Proc. Natl. Acad. Sci. U S A *79*, 4352–4356.

Blankenship, R.E. (2002). Molecular Mechanisms of Photosynthesis (Blackwell Science Ltd).

Burrows, P.A., Sazanov, L.A., Svab, Z., Maliga, P., and Nixon, P.J. (1998). Identification of a functional respiratory complex in chloroplasts through analysis of tobacco mutants containing disrupted plastid *ndh* genes. EMBO J. *17*, 868–876.

Cardol, P., Bailleul, B., Rappaport, F., Derelle, E., Béal, D., Breyton, C., Bailey, S., Wollman, F.A., Grossman, A., Moreau, H., and Finazzi, G. (2008). An original adaptation of photosynthesis in the marine green alga *Ostreococcus*. Proc. Natl. Acad. Sci. U S A *105*, 7881–7886.

Cheng, Z., Sun, L., Qi, T., Zhang, B., Peng, W., Liu, Y., and Xie, D. (2011). The bHLH transcription factor MYC3 interacts with the jasmonate ZIM-domain proteins to mediate jasmonate response in Arabidopsis. Mol. Plant *4*, 279–288.

Clark, R.D., Hawkesford, M.J., Coughlan, S.J., Bennett, J., and Hind, G. (1984). Association of ferredoxin-NADP+ oxidoreductase with the chloroplast cytochrome *b-f* complex. FEBS Lett. *174*, 137–142.

Cornic, G., and Fresneau, C. (2002). Photosynthetic carbon reduction and carbon oxidation cycles are the main electron sinks for photosystem II activity during a mild drought. Ann. Bot. *89*, 887–894.

DalCorso, G., Pesaresi, P., Masiero, S., Aseeva, E., Schünemann, D., Finazzi, G., Joliot, P., Barbato, R., and Leister, D. (2008). A complex containing PGRL1 and PGR5 is involved in the switch between linear and cyclic electron flow in Arabidopsis. Cell *132*, 273–285.

Daltrop, O., Allen, J.W.A., Willis, A.C., and Ferguson, S.J. (2002). *In vitro* formation of a *c*-type cytochrome. Proc. Natl. Acad. Sci. U S A *99*, 7872–7876.

Demmig-Adams, B., and Adams, W.W. (1992). Photoprotection and other responses of plants to high light stress. Annu. Rev. Plant Physiol. Plant Mol. Biol. *43*, 599–626.

Di Tommaso, P., Moretti, S., Xenarios, I., Orobitg, M., Montanyola, A., Chang, J.-M., Taly, J.-F., and Notredame, C. (2011). T-Coffee: a web server for the multiple sequence alignment of protein and RNA sequences using structural information and homology extension. Nucleic Acids Res. *39*, W13–W17.

Dizicheh, Z.B., Halloran, N., Asma, W., and Ghirlanda, G. (2017). De novo design of iron–sulfur proteins. Methods Enzymol. *595*, 33–53, First Edition.

Dunand, C., Mathé, C., Lazzarotto, F., Margis, R., and Margis-Pinheiro, M. (2011). Ascorbate peroxidase-related (APx-R) is not a duplicable gene. Plant Signal. Behav. *6*, 1908–1913.

Eisen, M.B., Spellman, P.T., Brown, P.O., and Botstein, D. (1998). Cluster analysis and display of genome-wide expression patterns. Proc. Natl. Acad. Sci. U S A *95*, 14863–14868.

Emanuelsson, O., Nielsen, H., and Heijne, G. Von (1999). ChloroP, a neural network-based method for predicting chloroplast transit peptides and their cleavage sites. Protein Sci. *8*, 978–984.

Endo, T., Shikanai, T., Takabayashi, A., Asada, K., and Sato, F. (1999). The role of chloroplastic NAD(P)H dehydrogenase in photoprotection. FEBS Lett. *457*, 5–8.

Fernández-Calvo, P., Chini, A., Fernández-Barbero, G., Chico, J.M., Gimenez-Ibanez, S., Geerinck, J., Eeckhout, D., Schweizer, F., Godoy, M., Franco-Zorrilla, J.M., et al. (2011). The Arabidopsis bHLH transcription factors MYC3 and MYC4 are targets of JAZ repressors and act additively with MYC2 in the activation of jasmonate responses. Plant Cell *23*, 701–715.

Ferro, M., Brugière, S., Salvi, D., Seigneurin-Berny, D., Court, M., Moyet, L., Ramus, C., Miras, S., Mellal, M., Le Gall, S., et al. (2010). AT_CHLORO, a comprehensive chloroplast proteome database with subplastidial localization and curated information on envelope proteins. Mol. Cell. Proteomics *9*, 1063–1084.

Fisher, N., and Kramer, D.M. (2014). Non-photochemical reduction of thylakoid photosynthetic redox carriers *in vitro*: relevance to cyclic electron flow around photosystem I? Biochim. Biophys. Acta *1837*, 1944–1954.

Freibert, S.A., Weiler, B.D., Bill, E., Pierik, A.J., Mühlenhoff, U., and Lill, R. (2018). Biochemical reconstitution and spectroscopic analysis of iron–sulfur proteins. Methods Enzymol. *599*, 197–226.

Ghysels, B., Godaux, D., Matagne, R.F., Cardol, P., and Franck, F. (2013). Function of the chloroplast hydrogenase in the microalga *Chlamydomonas*: the role of hydrogenase and state transitions during photosynthetic activation in anaerobiosis. PLoS One *8*, e64161.

Goss, T., and Hanke, G. (2014). The end of the line: can ferredoxin and ferredoxin NADP(H) oxidoreductase determine the fate of photosynthetic electrons? Curr. Protein Pept. Sci. *15*, 385–393.

Gotoh, E., Matsumoto, M., Ogawa, K., Kobayashi, Y., and Tsuyama, M. (2010). A qualitative analysis of the regulation of cyclic electron flow around photosystem I from the post-illumination chlorophyll fluorescence transient in Arabidopsis: a new platform for the in vivo investigation of the chloroplast redox state. Photosynth. Res. *103*, 111–123.

Govindjee, Shevela, D., and Björn, L.O. (2017). Evolution of the Z-scheme of photosynthesis: a perspective. Photosynth. Res. *133*, 5–15.

Guan, X., Chen, S., Voon, C.P., Wong, K.-B., Tikkanen, M., and Lim, B.L. (2018). FdC1 and leaf-type ferredoxins channel electrons from Photosystem I to different downstream electron acceptors. Front. Plant Sci. *9*, 410.

Harada, K., Arizono, T., Sato, R., Trinh, M.D.L., Hashimoto, A., Kono, M., Tsujii, M., Uozumi, N., Takaichi, S., and Masuda, S. (2019). DAY-LENGTH-DEPENDENT DELAYED-GREENING1, the Arabidopsis homolog of the cyanobacterial H^+-extrusion protein, is essential for chloroplast pH regulation and optimization of non-photochemical quenching. Plant Cell Physiol. *60*, 2660–2671.

Heyno, E., Gross, C.M., Laureau, C., Culcasi, M., Pietri, S., and Krieger-Liszky, A. (2009). Plastid alternative oxidase (PTOX) promotes oxidative stress when overexpressed in tobacco. J. Biol. Chem. *284*, 31174–31180.

Honma, T., and Goto, K. (2001). Complexes of MADS-box proteins are sufficient to convert leaves into floral organs. Nature *409*, 525–529.

Hoppe, A., Pandelia, M.E., Gärtner, W., and Lubitz, W. (2011). $[Fe_4S_4]$- and $[Fe_3S_4]$-cluster formation in synthetic peptides. Biochim. Biophys. Acta *1807*, 1414–1422.

Houille-Vernes, L., Rappaport, F., Wollman, F.A., Alric, J., and Johnson, X. (2011). Plastid terminal oxidase 2 (PTOX2) is the major oxidase involved in chlororespiration in *Chlamydomonas*. Proc. Natl. Acad. Sci. U S A *108*, 20820–20825.

Ibrahim, I.M., Wu, H., Ezhov, R., Kayanja, G.E., Zakharov, S.D., Du, Y., Tao, W.A., Pushkar, Y., Cramer, W.A., and Puthiyaveetil, S. (2020). An evolutionarily conserved iron-sulfur cluster underlies redox sensory function of the chloroplast sensor kinase. Commun. Biol. *3*, 1–11.

Johnson, G.N. (2011). Physiology of PSI cyclic electron transport in higher plants. Biophys. Biochim. Acta *1807*, 384–389.

Joliot, P., and Johnson, G.N. (2011). Regulation of cyclic and linear electron flow in higher plants. Proc. Natl. Acad. Sci. U S A *108*, 13317–13322.

Joliot, P., and Joliot, A. (2006). Cyclic electron flow in C3 plants. Biochim. Biophys. Acta *1757*, 362–368.

Kamruzzaman Munshi, M., Kobayashi, Y., and Shikanai, T. (2005). Identification of a novel protein, CRR7, required for the stabilization of the chloroplast NAD(P)H dehydrogenase complex in Arabidopsis. Plant J. *44*, 1036–1044.

Kannchen, D., Zabret, J., Oworah-nkruma, R., Dyczmons-nowaczyk, N., Wiegand, K., Löbbert, P., Frank, A., Nowaczyk, M.M., Rexroth, S., and Rögner, M. (2020). Remodeling of photosynthetic electron transport in *Synechocystis* sp . PCC 6803 for future hydrogen production from water. Biochim. Biopys. Acta *1861*, 148208.

Kennedy, M.C., Kent, T.A., Emptage, M., Merkle, H., Beinert, H., and Münck, E. (1984). Evidence for the formation of a linear [3Fe-4S] cluster in partially unfolded aconitase. J. Biol. Chem. *259*, 14463–14471.

Kono, M., Yamori, W., Suzuki, Y., and Terashima, I. (2017). Photoprotection of PSI by far-red light against the fluctuating light-induced photoinhibition in *Arabidopsis thaliana* and field-grown plants. Plant Cell Physiol *58*, 35–45.

Kudoh, H., and Sonoike, K. (2002). Irreversible damage to photosystem I by chilling in the light: cause of the degradation of chlorophyll after returning to normal growth temperature. Planta *215*, 541–548.

Lee, J., Oh, M., Park, H., and Lee, I. (2008). SOC1 translocated to the nucleus by interaction with AGL24 directly regulates LEAFY. Plant J. *55*, 832–843.

Li, J., Ren, X., Fan, B., Huang, Z., Wang, W., Zhou, H., Lou, Z., Ding, H., Lyu, J., and Tan, G. (2019). Zinc toxicity and iron-sulfur cluster biogenesis in *Escherichia coli*. Appl. Environ. Microbiol. *85*, 01967–18.

Li, X., Sui, X., Zhao, W., Huang, H., Chen, Y., and Zhang, Z. (2015). Characterization of cucumber violaxanthin de-epoxidase gene promoter in Arabidopsis. J. Biosci. Bioeng. *119*, 470–477.

Li, X., Zhao, W., Sun, X., Huang, H., Kong, L., Niu, D., Sui, X., and Zhang, Z. (2013). Molecular cloning and characterization of violaxanthin de-epoxidase (CsVDE) in Cucumber. PLoS One *8*, 1–11.

Li, Z., Peers, G., Dent, R.M., Bai, Y., Yang, S.Y., Apel, W., Leonelli, L., and Niyogi, K.K. (2016). Evolution of an atypical de-epoxidase for photoprotection in the green lineage. Nat. Plants *2*, 16140.

Li, Z., Wakao, S., Fischer, B.B., and Niyogi, K.K. (2009). Sensing and responding to excess light. Annu. Rev. Plant Biol. *60*, 239–260.

Lippard, S.J., and Berg, J.M. (1994). Principles of Bioinorganic Chemistry (University Science Books).

Liu, C., Chen, H., Er, H.L., Soo, H.M., Kumar, P.P., Han, J.H., Liou, Y.C., and Yu, H. (2008). Direct interaction of AGL24 and SOC1 integrates flowering signals in Arabidopsis. Development *135*, 1481–1491.

Long, T.A., Okegawa, Y., Shikanai, T., Schmidt, G.W., and Covert, S.F. (2008). Conserved role of PROTON GRADIENT REGULATION 5 in the regulation of PSI cyclic electron transport. Planta *228*, 907–918.

Mai Duy Luu, T., Sato, R., and Masuda, S. (2018). Genetic characterization of a *flap1* null mutation in Arabidopsis *npq4* and *pgr5* plants suggests that the regulatory role of FLAP1 involves control of proton homeostasis in chloroplasts. Photosynth. Res. *139*, 413–424.

Mezulis, S., Yates, C.M., Wass, M.N., E Sternberg, M.J., and Kelley, L.A. (2015). The Phyre2 web portal for protein modeling, prediction and analysis. Nat. Protoc. *10*, 845–858.

Munekage, Y., Hashimoto, M., Miyake, C., Tomizawa, K.-I., Endo, T., Tasaka, M., and Shikanai, T. (2004). Cyclic electron flow around photosystem I is essential for photosynthesis. Nature *429*, 579–582.

Munekage, Y., Hojo, M., Meurer, J., Endo, T., Tasaka, M., and Shikanai, T. (2002). PGR5 is involved in cyclic electron flow around photosystem I and is essential for photoprotection in Arabidopsis. Cell *110*, 361–371.

Munekage, Y., and Shikanai, T. (2005). Cyclic electron transport through photosystem I. Plant Biotechnol. *22*, 361–369.

Nagarajan, A., Page, L.E., Liberton, M., and Pakrasi, H.B. (2014). Consequences of decreased light harvesting capability on photosystem II function in *Synechocystis* sp. PCC 6803. Life *4*, 903–914.

Nakamaru-Ogiso, E., Yano, T., Ohnishi, T., and Yagi, T. (2002). Characterization of the iron-sulfur cluster coordinated by a cysteine cluster motif(CXXCXXXCX27C) in the Nqo3 subunit in the proton-translocating NADH-quinone oxidoreductase (NDH-1) of *Thermus thermophilus* HB-8. J. Biol. Chem. *277*, 1680–1688.

Nanda, V., Senn, S., Pike, D.H., Rodriguez-Granillo, A., Hansen, W., Khare, S.D., and Noyc, D. (2016). Structural principles for computational and de novo design of 4Fe-4S metalloproteins. Biochim. Biophys. Acta *1857*, 531–538.

Nandha, B., Finazzi, G., Joliot, P., Hald, S., and Johnson, G.N. (2007). The role of PGR5 in the redox poising of photosynthetic electron transport. Biochim. Biophys. Acta *1767*, 1252–1259.

Nawrocki, W.J., Bailleul, B., Cardol, P., Rappaport, F., Wollman, F.A., and Joliot, P. (2019a). Maximal cyclic electron flow rate is independent of PGRL1 in *Chlamydomonas*. Biochim. Biophys. Acta *1860*, 425–432.

Nawrocki, W.J., Bailleul, B., Picot, D., Cardol, P., Rappaport, F., Wollman, F.-A., and Joliot, P. (2019b). The mechanism of cyclic electron flow. Biochim. Biophys. Acta *1860*, 433–438.

Nawrocki, Wojciech J., Buchert, F., Joliot, P., Rappaport, F., Bailleul, B., and Wollman, F.A. (2019c). Chlororespiration controls growth under intermittent light. Plant Physiol. *179*, 630–639.

Nikkanen, L., Toivola, J., Trotta, A., Diaz, M.G., Tikkanen, M., Aro, E.M., and Rintamäki, E. (2018). Regulation of cyclic electron flow by chloroplast NADPH-dependent thioredoxin system. Plant Direct *2*, 1–24.

Nishio, J.N., and Whitmarsh, J. (1993). Dissipation of the proton electrochemical potential in intact chloroplasts II . The pH gradient monitored by cytochrome *f* reduction kinetics. Plant Physiol. *101*, 89–96.

Niyogi, K.K., and Truong, T.B. (2013). Evolution of flexible non-photochemical quenching mechanisms that regulate light harvesting in oxygenic photosynthesis. Curr. Opin. Plant Biol. *16*, 307–314.

Notredame, C., Higgins, D.G., and Heringa, J. (2000). T-coffee: a novel method for fast and accurate multiple sequence alignment. J. Mol. Biol. *302*, 205–217.

Okegawa, Y., Kagawa, Y., Kobayashi, Y., and Shikanai, T. (2008). Characterization of factors affecting the activity of photosystem I cyclic electron transport in chloroplasts. Plant Cell Physiol. *49*, 825–834.

Okegawa, Y., Long, T.A., Iwano, M., Takayama, S., Kobayashi, Y., Covert, S.F., and Shikanai, T. (2007). A balanced PGR5 level is required for chloroplast development and optimum operation of cyclic electron transport around photosystem I. Plant Cell Physiol. *48*, 1462–1471.

Okegawa, Y., and Motohashi, K. (2020). M-type thioredoxins regulate the PGR5/PGRL1-dependent pathway by forming a disulfide-linked complex with PGRL1. Plant Cell *32*, 3866–3883.

Pelaz, S., Ditta, G.S., Baumann, E., Wisman, E., and Yanofsky, M.F. (2000). B and C floral organ identity functions require SEPALLATTA MADS-box genes. Nature *405*, 200–203.

Ptushenko, V.V., Zhigalova, T.V., Avercheva, O.V., and Tikhonov, A.N. (2019). Three phases of energy-dependent induction of $P700^+$ and Chl a fluorescence in *Tradescantia fluminensis* leaves. Photosynth. Res. *139*, 509–522.

Rosso, D., Ivanov, A.G., Fu, A., Geisler-Lee, J., Hendrickson, L., Geisler, M., Stewart, G., Krol, M., Hurry, V., Rodermel, S.R., et al. (2006). IMMUTANS does not act as a stress-induced safety valve in the protection of the photosynthetic apparatus of Arabidopsis during steady-state photosynthesis. Plant Physiol. *142*, 574–585.

Sato, R., Kono, M., Harada, K., Ohta, H., Takaichi, S., and Masuda, S. (2017). Fluctuating-light-acclimation protein1, conserved in oxygenic phototrophs, regulates H^+ homeostasis and non-photochemical quenching in chloroplasts. Plant Cell Physiol. *58*, 1622–1630.

Scheibe, R., Backhausen, J.E., Emmerlich, V., and Holtgrefe, S. (2005). Strategies to maintain redox homeostasis during photosynthesis under changing conditions. J. Exp. Bot. *56*, 1481–1489.

Schweizer, F., Fernández-Calvo, P., Zander, M., Diez-Diaz, M., Fonseca, S., Glauser, G., Lewsey, M.G., Ecker, J.R., Solano, R., and Reymond, P. (2013). Arabidopsis basic helix-loop-helix transcription factors MYC2,MYC3, andMYC4 regulate glucosinolate biosynthesis, insect performance, and feeding behavior. Plant Cell *25*, 3117–3132.

Shaku, K., Shimakawa, G., Hashiguchi, M., and Miyake, C. (2016). Reduction-induced suppression of electron flow (RISE) in the photosynthetic electron transport system of *Synechococcus elongatus* PCC 7942. Plant Cell Physiol *57*, 1443–1453.

Shikanai, T. (2007). Cyclic electron transport around photosystem I: genetic approaches. Annu. Rev. Plant Biol. *58*, 199–217.

Shikanai, T., Endo, T., Hashimoto, T., Yamada, Y., Asada, K., and Yokota, A. (1998). Directed disruption of the tobacco *ndhB* gene impairs cyclic electron flow around photosystem I. Proc. Natl. Acad. Sci. U S A *95*, 9705–9709.

Shimada, H., Mochizuki, M., Ogura, K., Froehlich, J.E., Osteryoung, K.W., Shirano, Y., Shibata, D., Masuda, S., Mori, K., and Takamiya, K.-I. (2007). Arabidopsis cotyledon-specific chloroplast biogenesis factor CYO1 is a protein disulfide isomerase. Plant Cell *19*, 3157–3169.

Shimakawa, G., and Miyake, C. (2018a). Oxidation of P700 ensures robust photosynthesis. Front. Plant Sci. *9*, 1–15.

Shimakawa, G., and Miyake, C. (2018b). Changing frequency of fluctuating light reveals the molecular mechanism for P700 oxidation in plant leaves. Plant Direct *2*, 1–11.

Shimakawa, G., Shaku, K., and Miyake, C. (2018). Reduction-induced suppression of electron flow (RISE) is relieved by non-ATP-consuming electron flow in *Synechococcus elongatus* PCC 7942. Front. Microbiol. *9*, 1–11.

Smolen, G.A., Pawlowski, L., Wilensky, S.E., and Bender, J. (2002). Dominant alleles of the basic helix-loop-helix transcription factor ATR2 activate stress-responsive genes in Arabidopsis. Genetics *161*, 1235–1246.

Somersalo, S., and Krause, G.H. (1989). Photoinhibition at chilling temperature - fluorescence characteristics of unhardened and cold-acclimated spinach leaves. Planta *177*, 409–416.

Sonoike, K. (2011). Photoinhibition of photosystem I. Physiol. Plant *142*, 56–64.

Steinbeck, J., Ross, I.L., Rothnagel, R., Gäbelein, P., Schulze, S., Giles, N., Ali, R., Drysdale, R., Sierecki, E., Gambin, Y., et al. (2018). Structure of a PSI-LHCI-cyt b_6f supercomplex in *Chlamydomonas reinhardtii* promoting cyclic electron flow under anaerobic conditions. Proc. Natl. Acad. Sci. U S A *115*, 10517–10522.

Suorsa, M., Järvi, S., Grieco, M., Nurmi, M., Pietrzykowska, M., Rantala, M., Kangasjärvi, S., Paakkarinen, V., Tikkanen, M., Jansson, S., et al. (2012). PROTON GRADIENT REGULATION5 is essential for proper acclimation of Arabidopsis photosystem I to naturally and artificially fluctuating light conditions. Plant Cell *24*, 2934–2948.

Surerus, K.K., Kennedy, M.C., Beinert, H., and Munck, E. (1989). Mossbauer study of the inactive Fe_3S_4 and Fe_3Se_4 and the active Fe_4Se_4 forms of beef heart aconitase. Proc. Natl. Acad. Sci. U S A *86*, 9846–9850.

Szklarczyk, D., Franceschini, A., Wyder, S., Forslund, K., Heller, D., Huerta-Cepas, J., Simonovic, M., Roth, A., Santos, A., Tsafou, K.P., et al. (2015). STRING v10: protein-protein interaction networks, integrated over the tree of life. Nucleic Acids Res. *43*, D447–D452.

Takabayashi, A., Ishikawa, N., Obayashi, T., Ishida, S., Obokata, J., Endo, T., and Sato, F. (2009). Three novel subunits of Arabidopsis chloroplastic NAD(P)H dehydrogenase identified by bioinformatic and reverse genetic approaches. Plant J. *57*, 207–219.

Takagi, D., and Miyake, C. (2018). Proton gradient regulation 5 supports linear electron flow to oxidize photosystem I. Physiol. Plant *164*, 337–348.

Talts, E., Oja, V., Rämma, H., Rasulov, B., Anijalg, A., and Laisk, A. (2007). Dark inactivation of ferredoxin-NADP reductase and cyclic electron flow under far-red light in sunflower leaves. Photosynth. Res. *94*, 109–120.

Telser, J., Lee, H.I., and Hoffman, B.M. (2000). Investigation of exchange couplings in $[Fe_3S_4]^+$ clusters by electron spin-lattice relaxation. J. Biol. Inorg. Chem. *5*, 369–380.

Terashima, M., Petroutsos, D., Hüdig, M., Tolstygina, I., Trompelt, K., Gäbelein, P., Fufezan, C., Kudla, J., Weinl, S., Finazzi, G., and Hippler, M. (2012). Calcium-dependent regulation of cyclic photosynthetic electron transfer by a CAS, ANR1, and PGRL1 complex. Proc. Natl. Acad. Sci. U S A *109*, 17717–17722.

Tikhonov, A.N. (2013). pH-dependent regulation of electron transport and ATP synthesis in chloroplasts. Photosynth. Res. *116*, 511–534.

Timmis, J.N., Ayliff, M.A., Huang, C.Y., and Martin, W. (2004). Endosymbiotic gene transfer: organelle genomes forge eukaryotic chromosomes. Nat. Rev. Genet. *5*, 123–135.

Tiwari, A., Mamedov, F., Grieco, M., Suorsa, M., Jajoo, A., Styring, S., Tikkanen, M., and Aro, E.M. (2016). Photodamage of iron-sulphur clusters in

photosystem I induces non-photochemical energy dissipation. Nat. Plants *2*, 16035.

van Dam, S., Võsa, U., van der Graaf, A., Franke, L., and de Magalhães, J.P. (2018). Gene co-expression analysis for functional classification and gene-disease predictions. Brief. Bioinform. *19*, 575–592.

Voss, I., Goss, T., Murozuka, E., Altmann, B., McLean, K.J., Rigby, S.E.J., Munro, A.W., Scheibe, R., Hase, T., and Hanke, G.T. (2011). FdC1, a novel ferredoxin protein capable of alternative electron partitioning, increases in conditions of acceptor limitation at photosystem I. J. Biol. Chem. *286*, 50–59.

Wada, S., Suzuki, Y., Takagi, D., Miyake, C., and Makino, A. (2018). Effects of genetic manipulation of the activity of photorespiration on the redox state of photosystem I and its robustness against excess light stress under CO_2-limited conditions in rice. Photosynth. Res. *137*, 431–441.

Walker, M.G., Volkmuth, W., Sprinzak, E., Hodgson, D., and Klingler, T. (1999). Prediction of gene function by genome-scale expression analysis: prostate cancer-associated genes. Genome Res. *9*, 1198–1203.

Woehle, C., Dagan, T., Landan, G., Vardi, A., and Rosenwasser, S. (2017). Expansion of the redox-sensitive proteome coincides with the plastid endosymbiosis. Nat. Plants *3*, 17066.

Xu, D., and Zhang, Y. (2013). Toward optimal fragment generations for ab initio protein structure assembly. Proteins Struct. Funct. Bioinforma. *81*, 229–239.

Xu, D., and Zhang, Y. (2012). Ab initio protein structure assembly using continuous structure fragments and optimized knowledge-based force field. Proteins *80*, 1715–1735.

Xu, Z., Mahmood, K., and Rothstein, S.J. (2017). ROS induces anthocyanin production via late biosynthetic genes and anthocyanin deficiency confers the hypersensitivity to ROS-generating stresses in Arabidopsis. Plant Cell Physiol. *58*, 1364–1377.

Yabe, T., Morimoto, K., Kikuchi, S., Nishio, K., Terashima, I., and Nakaia, M. (2004). The Arabidopsis chloroplastic NifU-like protein CnfU, which can act as an iron-sulfur cluster scaffold protein, is required for biogenesis of ferredoxin and photosystem I. Plant Cell *16*, 993–1007.

Yadav, K.N.S., Semchonok, D.A., Nosek, L., Kouřil, R., Fucile, G., Boekema, E.J., and Eichacker, L.A. (2017). Supercomplexes of plant photosystem I with cytochrome b_6f, light-harvesting complex II and NDH. Biochim. Biophys. Acta *1858*, 12–20.

Yamamoto, H., Peng, L., Fukao, Y., and Shikanai, T. (2011). An Src homology 3 domain-like fold protein forms a ferredoxin binding site for the chloroplast NADH dehydrogenase-like complex in Arabidopsis. Plant Cell *23*, 1480–1493.

Yamori, W., and Shikanai, T. (2016). Physiological functions of cyclic electron transport around photosystem I in sustaining photosynthesis and plant growth. Annu. Rev. Plant Biol. *67*, 81–106.

Yin, L., Dragnea, V., Feldman, G., Hammad, L.A., Karty, J.A., Dann, C.E., and Bauer, C.E. (2013). Redox and light control the heme-sensing activity of AppA. MBio *4*, 1–9.

Zhang, H., Whitelegge, J.P., and Cramer, W.A. (2001). Ferredoxin:$NADP^+$ oxidoreductase is a subunit of the chloroplast cytochrome b_6f complex. J. Biol. Chem. *276*, 38159–38165.

Zhang, S., and Scheller, H.V. (2004). Photoinhibition of photosystem I at chilling temperature and subsequent recovery in *Arabidopsis thaliana*. Plant Cell Physiol. *45*, 1595–1602.

Zivcak, M., Brestic, M., Kunderlikova, K., Sytar, O., and Allakhverdiev, S.I. (2015). Repetitive light pulse-induced photoinhibition of photosystem i severely affects CO_2 assimilation and photoprotection in wheat leaves. Photosynth. Res. *126*, 449–463.

iScience, Volume *24*

Supplemental Information

The evolutionary conserved iron-sulfur protein TCR controls P700 oxidation in photosystem I

Mai Duy Luu Trinh, Daichi Miyazaki, Sumire Ono, Jiro Nomata, Masaru Kono, Hiroyuki Mino, Tatsuya Niwa, Yuki Okegawa, Ken Motohashi, Hideki Taguchi, Toru Hisabori, and Shinji Masuda

Table S1. Comparison of photosynthetic protein identified by Mass-Spectrometry analysis between *tcr* and WT. Related to Figure 6.

Protein complexes	Protein subunits	Fold change[a] (*tcr*/WT)	Fold change[b] (*tcr*/WT)
Photosystem II	CP43 (PsbC)	1.00	1.03
	CP47 (PsbB)	1.01	1.06
	D1 (PsbA)	0.99	1.02
	D2 (PsbD)	1.12	1.06
	PsbE	0.93	1.30
	PsbF	1.05	1.00
	PsbO	0.93	0.86
	PsbP	1.09	0.88
	PsbQ1	1.03	1.12
	PsbQ2	0.98	1.14
	PsbR	0.98	0.92
	PsbS	1.00	1.04
Cytochrome b_6f	PetD	1.74	0.85
Photosystem I	PsaA	0.97	0.99
	PsaB	1.00	1.06
	PsaC	0.91	1.01
	PsaD2	0.95	0.94
	PsaE1	0.87	0.95
	PsaF	1.03	1.27
	PsaG	0.86	1.23
	PsaH2	1.28	1.12
	PsaK	0.95	0.92
	PsaN	1.02	1.16
	PsaO	1.38	1.52
	Lhca2	1.06	1.60
	Lhca3	1.15	1.13
	FNRL1 (FNR)	0.96	0.94
	FNRL2 (FNR)	1.00	0.96
ATP synthase	ATPA	1.02	0.90
	ATPB	1.00	0.91
	ATPD	0.99	1.23
	ATPE	0.96	1.16
	ATPF	1.05	1.18
	ATPG1	1.01	1.02
	ATPG2	N.D.	0.85
	ATPH	0.88	1.35
	ATPI	1.37	1.37
Rubisco	RBL	1.10	1.10
	RBS1A	1.19	1.19
NDH complex	PnsB1	0.97	0.94
	PnsB2	0.98	0.91
	NDHH	N.D.	0.97
PGR5/PGRL1 complex	PGL1A	1.03	0.94
	STT7 (STN7)	1.03	1.20

[a] The first experimental replication, [b] The second experimental replication, **N.D**. No data

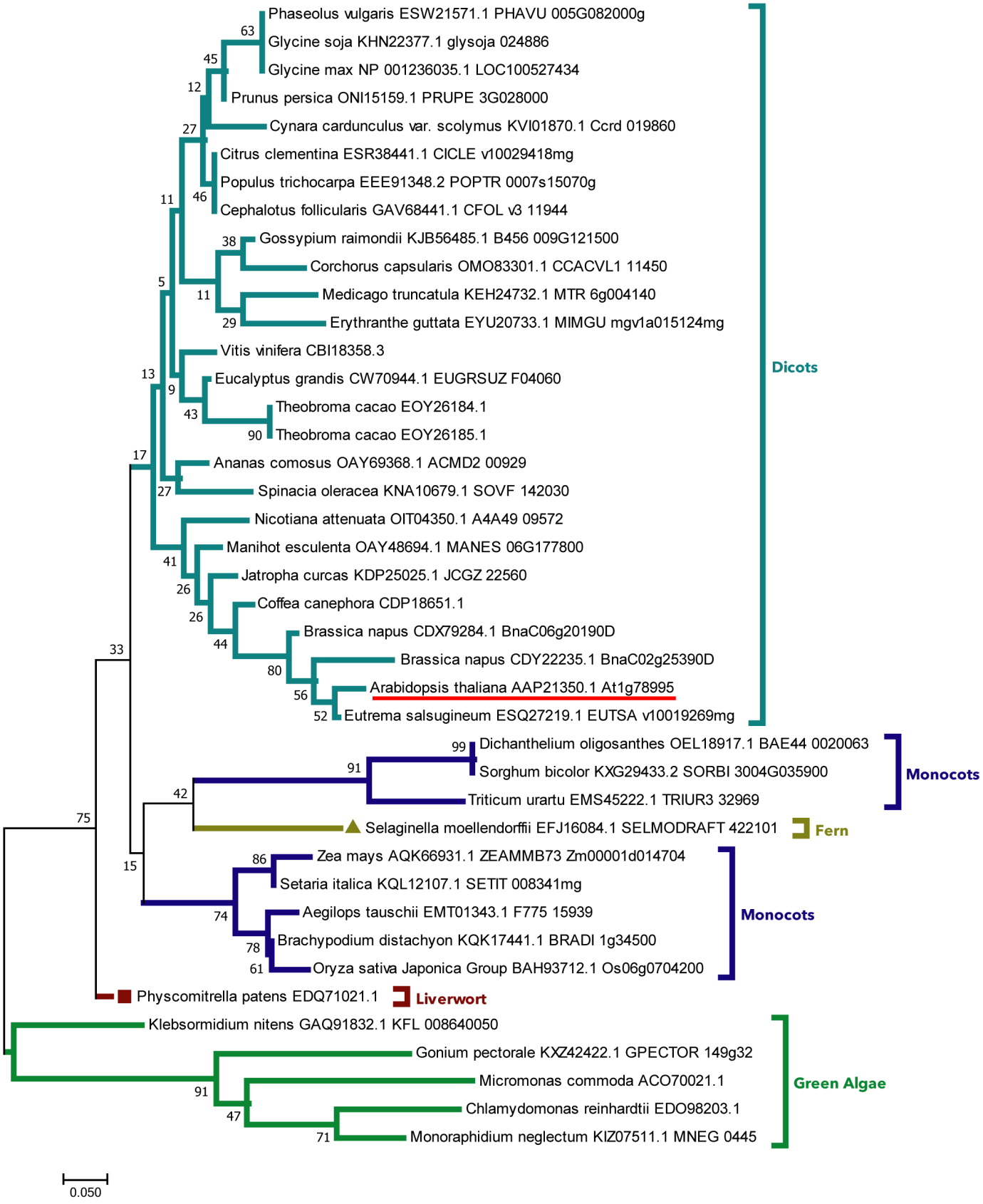

Figure S1. Evolutionary relationship between taxa and the phylogenetic tree of TCR homologs. Related to Figure 1.

The optimal tree with a sum of branch length of 3.66958327 is shown. The results of the bootstrap test (1000 replicates) are shown on branches. The tree was drawn to scale, with branch lengths indicated using the same units as those of the evolutionary distances that were used to infer the phylogenetic tree. The analysis involved 41 amino acid sequences. The final dataset included a total of 27 positions. Evolutionary analyses were conducted in MEGA7.

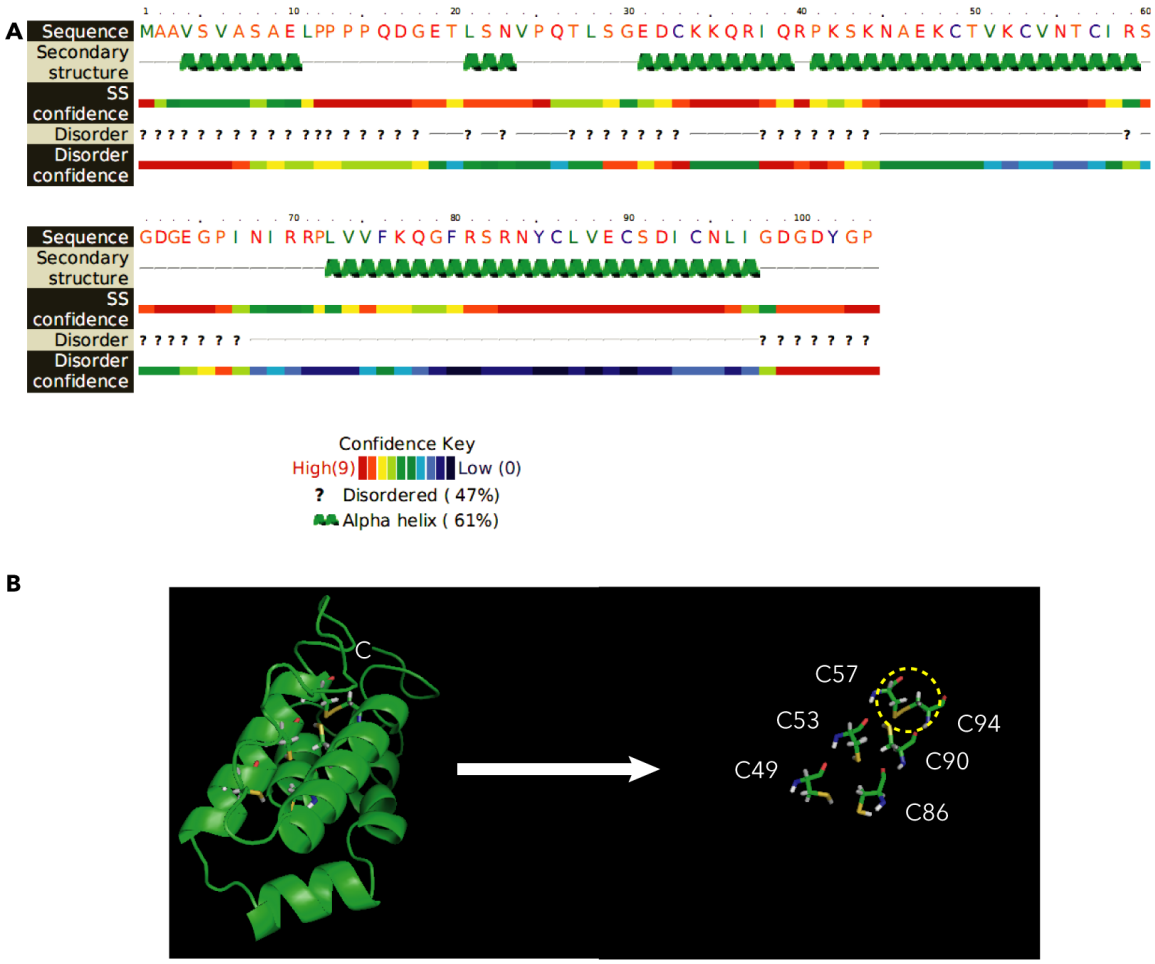

Figure S2. A predicted structure of TCR. Related to Figure 1.

(A) A predicted secondary structure of TCR, as assessed using Phyre2.

(B) The most probable tertiary structure of TCR, as revealed by the Ab initio structural modeling server (Xu and Zhang, 2013, 2012). The predicted disulfide bond is indicated by the yellow circle.

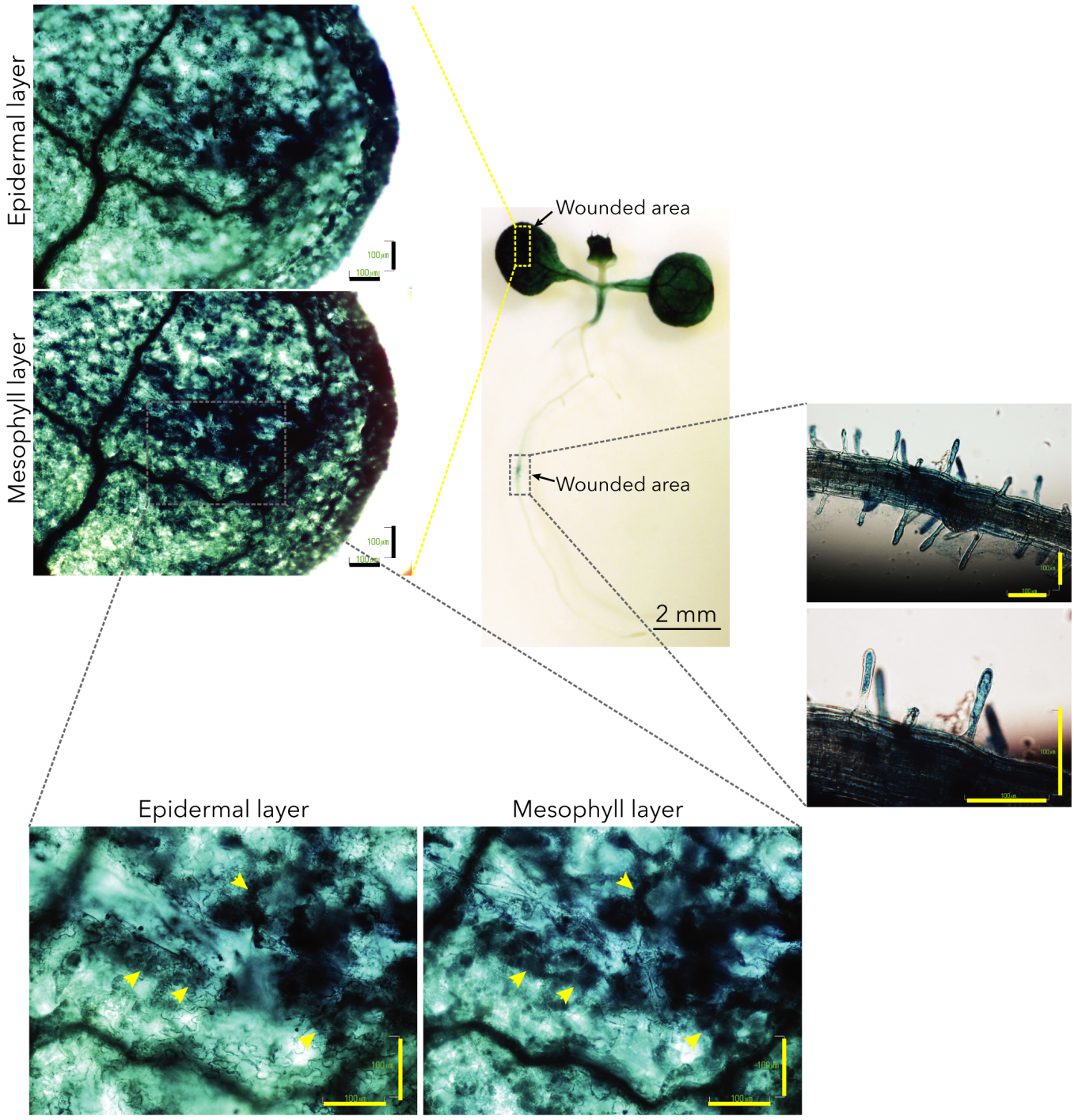

Figure S3. Histochemical analysis of GUS expression in a wounded 5-day-old transgenic plant. Related to Figure 5.

Observations of the leaf were focused on the epidermal layer, to determine the wounded area; subsequently, the focus was shifted to the mesophyll layer, to detect mesophyll cells that exhibited strong GUS expression. Yellow arrows, positions of mesophyll cells that showed strong GUS expression. Scale bar, 100 μm.

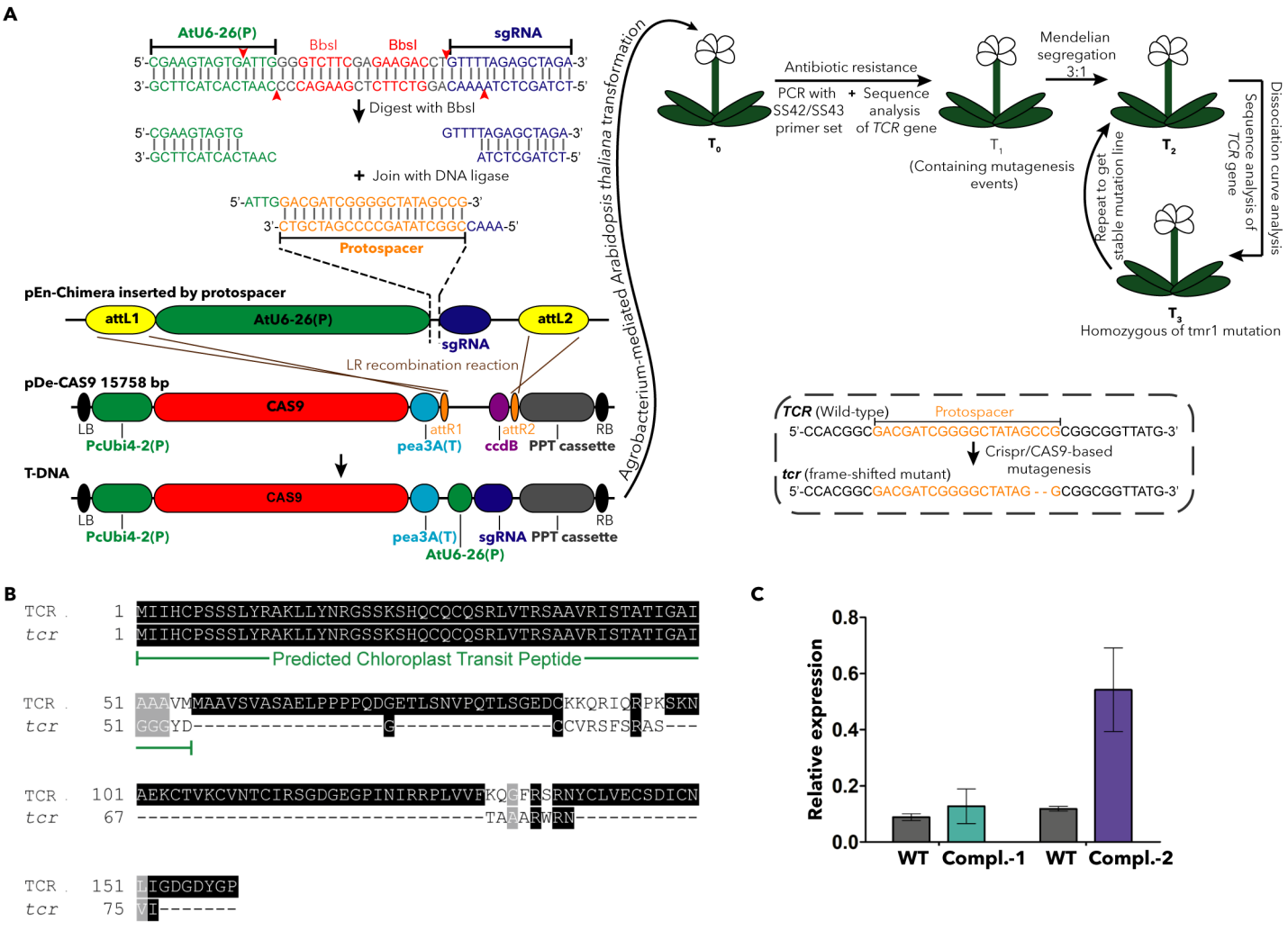

Figure S4. Preparation of *tcr* mutant and complementing lines. Related to Figure 6.

(A) Schematic representation of the experiment performed to isolate the *tcr* mutant. Experiments were performed according to previous reports (Fauser et al., 2014; Schiml et al., 2014).

(B) Amino acid sequence alignment of TCR from WT and *tcr* mutant plants.

(C) Relative expression levels of TCR in WT and complementing (Compl-1 and Compl-2) lines. Data are the mean ± SD (n = 3). The *actin* gene was used as an internal control.

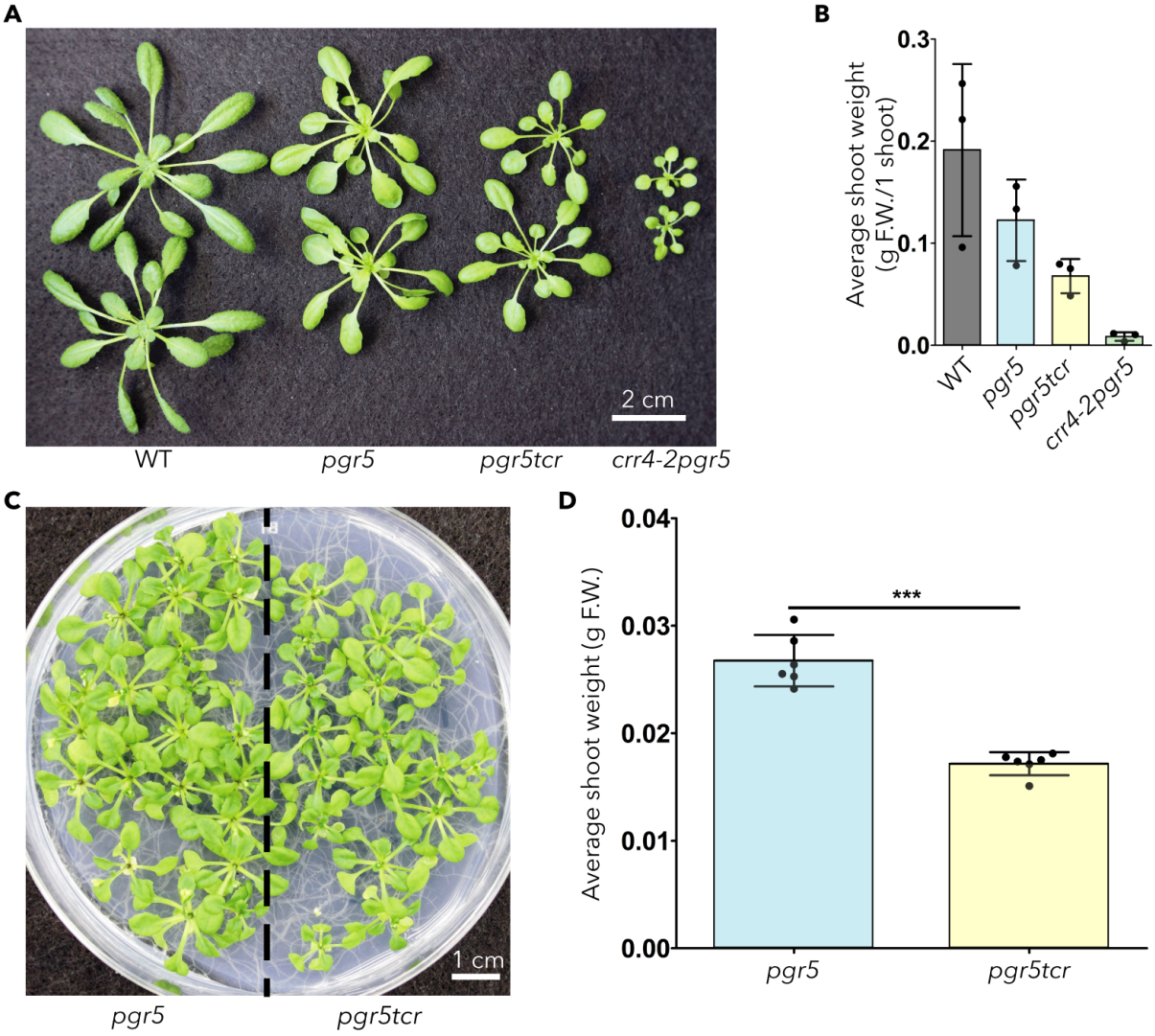

Figure S5. Phenotypic characterization of the *pgr5tcr* double mutant. Related to Figure 6.
(A) Shoot phenotype of WT and mutant plants grown on soil under short-day conditions for 37 days.
(B) Mean shoot weight of WT and mutant plants grown under the conditions indicated for panel (A). Data are the mean ± SD (n = 3).
(C) Shoot phenotype of *pgr5* and *pgr5tcr* plants grown on 1/2 MS agar under long-day conditions for 19 days.
(D) Mean shoot weight of *pgr5* and *pgr5tcr* plants grown under the conditions indicated for panel (C). Data are the mean ± SD (n = 5, with 10–16 plants per measurement). Statistically significant differences were analyzed as shown in the figure for the different types of plants using the two-tailed Student's *t*-test with a 95% CI (***$P < 0.001$). F.W., fresh weight.

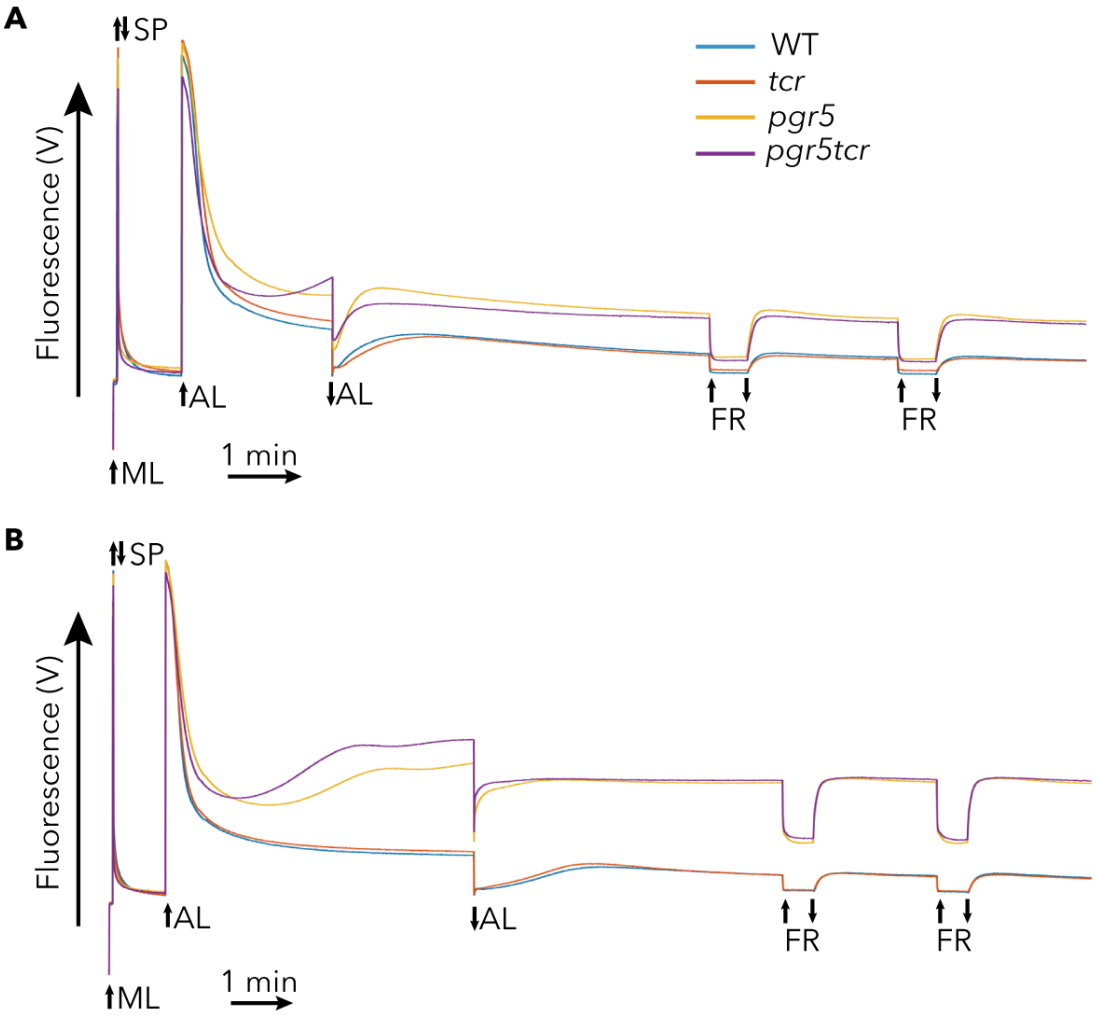

Figure S6. Fluorescence trace of PIFT analysis. Related to Figure 7.
(A) 2-min AL illumination was applied.
(B) 5-min AL illumination was applied.
↑, Light ON; ↓, light OFF; ML, measuring light; AL, red actinic light; FR, far-red light; ST, saturating pulse. All plants were grown under short-day conditions for 49–56 days on soil. Measurements were repeated three times and typical data are shown.

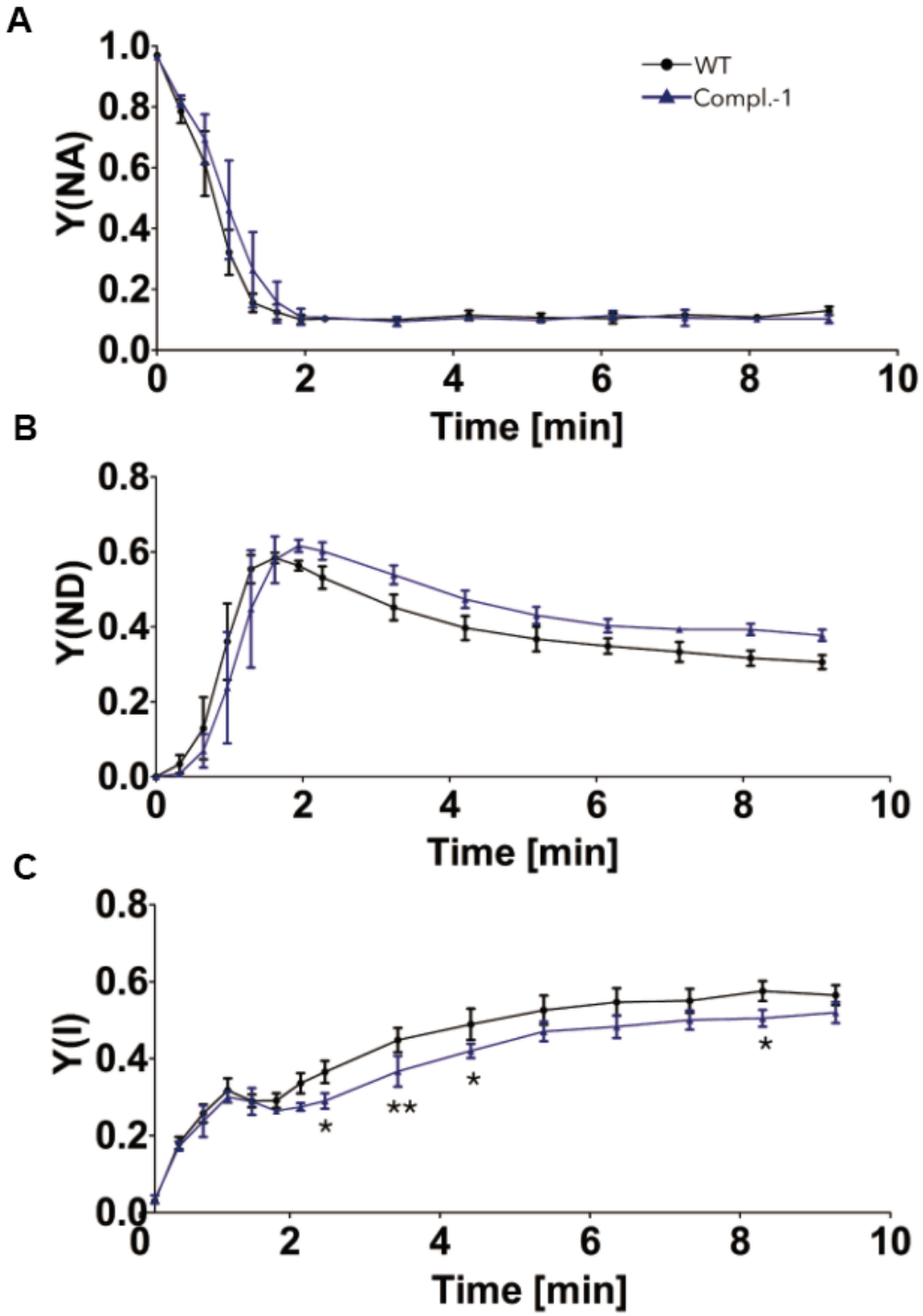

Figure S7. PSI activities of the Compl-1 line. Related to Figure 8.
Measurement of the accepter side limitation at PSI Y(NA) (A), the donor side limitation at PSI Y(YD) (B) and the PSI quantum yield Y(I) (C) in WT and the Compl-1 lines. **P* < 0.05, ***P* < 0.01 (one-way ANOVA followed by Tukey's test with a 95% CI). Growth and measuring conditions were shown in the legend of Figure 8C-F. Data represent the mean ± SD (n = 3).

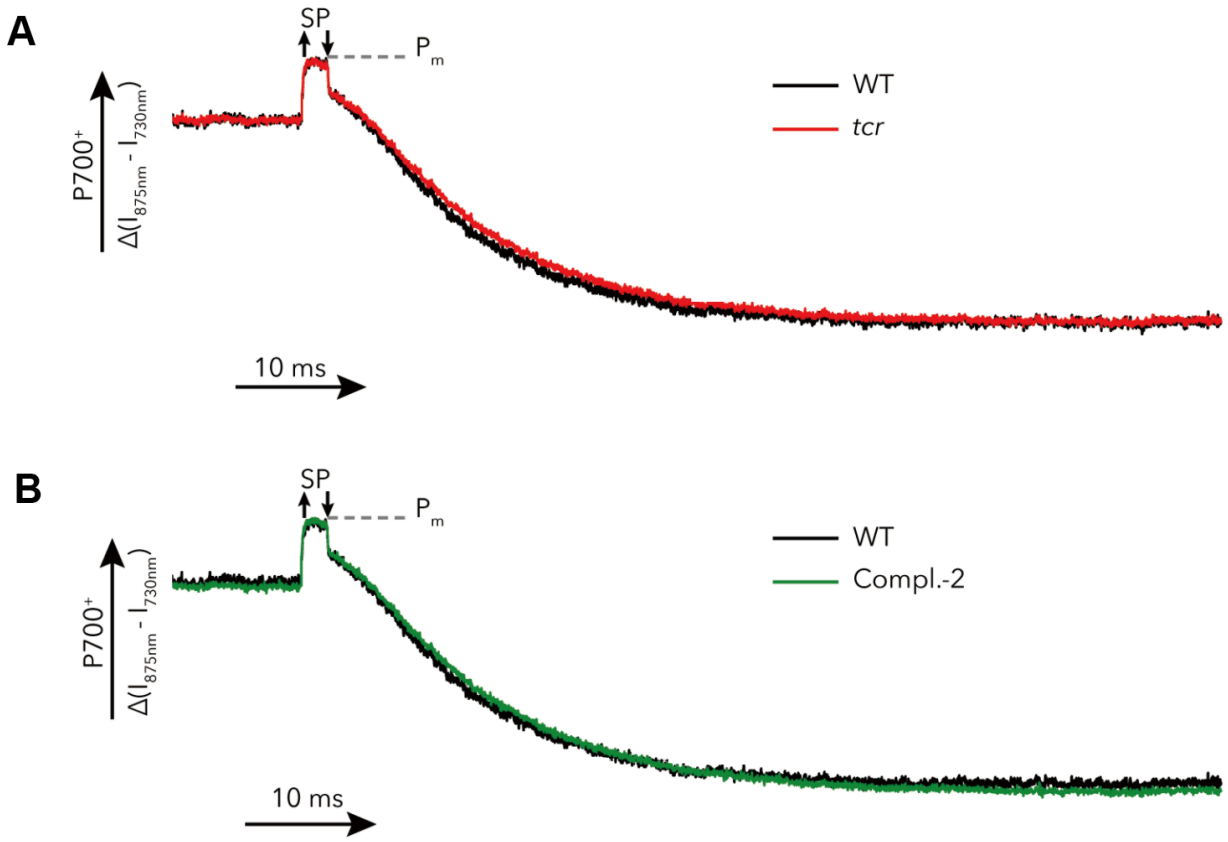

Figure S8. Measurement of P700 absorbance. Related to Figure 8.
Leaves were pre-illuminated by FR for 30 s then saturating pulse (SP) for 3 ms to fully oxidize P700. The decay of P700 signal resulted from the reduction of $P700^+$ by PC from Cyt b_6f. Data were presented to compare P700 kinetics between WT and tcr samples (A) or WT and Compl.-2 samples (B). Plants were grown on soil under short-day condition for 8 weeks. P700 ML = 10, FR light = 10, RT = 20 °C. Measurement was performed using Dual-PAM 100. Data were normalized to the maximum P700 oxidation (P_m).

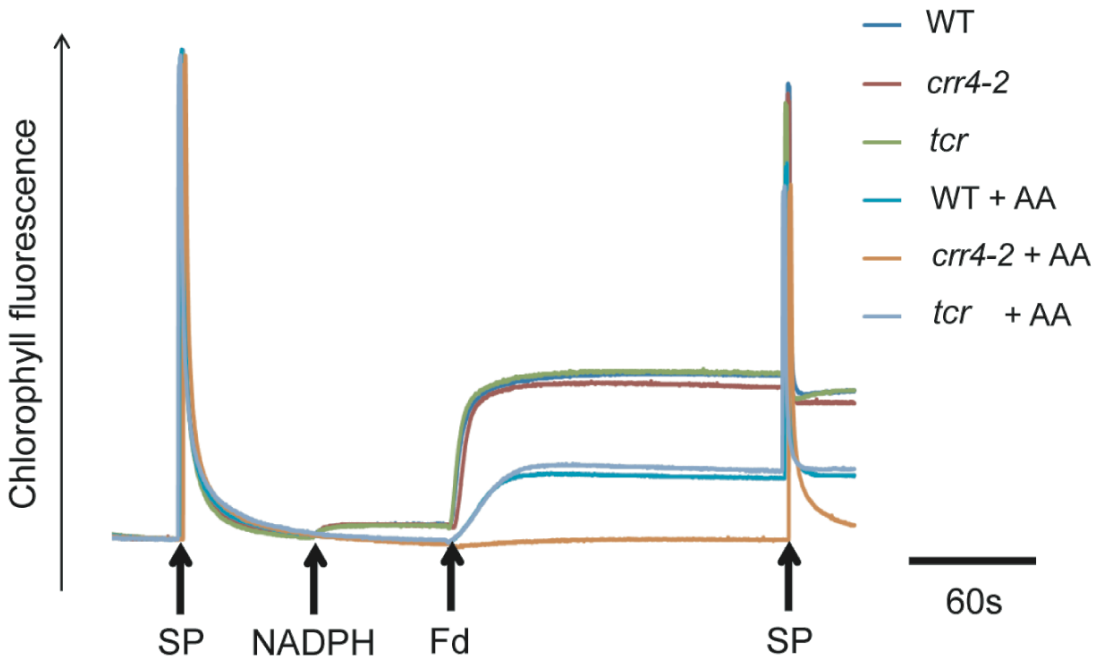

Figure S9. *In vitro* Fd-dependent PQ reduction in the ruptured chloroplasts isolated from WT and mutant plants. Related to Figure 9.

Fd-dependent PQ reduction activity was monitored as increments in chlorophyll fluorescence after the addition of NADPH (0.25 mM) and Fd (5 µM) under weak-light conditions (1.0 µmol photons m^{-2} s^{-1}). The fluorescence levels were normalized to Fm levels. To inhibit the PGR5-dependent PQ reduction, 10 µM antimycin A (AA) was added before the measurement.

Transparent Methods

Plant materials and growth conditions

The wild-type (WT) *A. thaliana* (L.) Heynh. ecotype Columbia (Col-0) and genetically modified mutants were used here, including a frameshifted knockout mutant of *TCR* (At1g78995; *tcr*), complementing lines of *tcr* (Compl-1 and Compl-2, Figure S4C), a T-DNA knockout mutant of *ndho* (At1g74880) (SALK_068922C) (Rumeau, 2004), a mutant of *pgr5* (At2g05620) (Munekage et al., 2002), a knockout mutant of a PPR gene (*crr4-2*) (Munekage et al., 2004), a *crr4-2pgr5* double mutant (Ifuku et al., 2011), a transgenic *A. thaliana* line expressing TCR fused with GFP (*35Spro::TCR-GFP*), and a transgenic *A. thaliana* line expressing GUS regulated by the *TCR* promoter (*TCRpro::GUS*). The details of the construction of the *tcr, 35Spro::TCR-GFP*, and *TCRpro::GUS* lines are provided below. *pgr5* and *crr4-2pgr5* mutant seeds were kindly provided by professor Toshiharu Shikanai at Kyoto University.

Plants were grown on agar containing a half-concentration of MS medium or soil (vermiculite:promix ratio of 1:1) under (1) constant light with an intensity of 39 μmol photons m^{-2} s^{-1} at 23°C, (2) short-day conditions (16 h dark (16°C)/8 h light (23°C) cycle, 110 μmol photons m^{-2} s^{-1}, 60 % relative humidity), or (3) long-day conditions (8 h dark (16°C)/16 h light (23°C) cycle, 40–50 μmol photons m^{-2} s^{-1}). Fluctuating- and FR-light illumination were conducted as described (Kono et al., 2017). Other conditions used here are indicated in the legend of each figure.

Construction of the *tcr* knockout mutant

The CRISPR/Cas9 system (Fauser et al., 2014; Schiml et al., 2014) was used here. The protospacer sequence (20 bp), which is specific to the At1g78995.1 locus (*TCR* gene), was selected from the CRISPR-PLANT (Xie et al., 2014). Moreover, potential off-target sequences of the selected protospacer sequence were checked using CHOPCHOP (Labun et al., 2016) and CCTop-CRISPR/Cas9 (Stemmer et al., 2015). The chosen protospacer sequence (5'–GACGATCGGGGCTATAGCCG–3') does not have any off-targeting sequences in the *A. thaliana* genome (Figure S4A). Next, this sequence was used to construct the *TCR*-targeted CRISPR/CAS9 expression vector (Figure S4A) according to Fauser et al., 2014 and Schiml et al., 2014. The pDe-CAS9 and pEn-Chimera plasmids were supported by Botaniches Institut II, Germany. All T_1 seeds harvested from T_0 plants were spread on agar containing 1/2MS and 12 μg/ml of D,L-phosphinothricin (PPT, Sigma). The T_1 plants that showed

resistance against PPT were chosen for checking the genomic insertion of the transgenic construct (CRISPR/CAS9-pDe-CAS9) by PCR using the SS42 (TCCCAGGATTAGAATGATTAGG) and SS43 (CGACTAAGGGTTTCTTATATGC) primers. The genomic sequence of *TCR* from the confirmed transgenic plants was amplified using the Myz-ATG-F (ATGATAATACACTGTCCTTCGTCATCTCTC) and Myz-STOP-R (TCAGGGACCATAGTCACCATCTCCGATCAA) primers, followed by Sanger sequencing. T_1 plants (n = 48; numbered from #1 to #48) showed DL-phosphinothricin resistance. Among the T_1 plants, 17 plants contained a genomic insertion of T-DNA (see Figure S4A for the T-DNA constructs): #4, #5, #6, #7, #8, #9, #10, #11, #12, #25, #27, #31, #38, #40, #43, #44, and #47. Only three of them (#5, #40, and #43; ~18 %) contained mutagenesis events. Based on Mendelian segregation, only plants #5 and #43 contained a single genomic T-DNA insertion. All T_1 plants containing mutagenesis events at the *TCR* gene were grown for harvesting T_2 seeds. About 150 seeds of each T_2 line were used to assess one Mendelian segregation on agar containing 1/2MS and 12 μg/ml of PPT (Griffiths et al., 2000). T_2 lines in which the Mendelian ratio was statistically equal to 3:1 were chosen for dissociation curve analysis via real-time PCR using the HRM-TCR-F (ATGATAATACACTGTCCTTCGTCATCTCTC) and HRM-TCR-R (GCGTTTGCGGTACGTTAGAT) primers. Some T_2 plants that showed abnormal dissociation curves compared with WT plants were selected for genomic sequence analysis of the *TCR* gene. If a homozygous mutant was detected, the genomic sequence of the *TCR* gene of the next two generations was checked, to guarantee that the heritable events were stable and CAS9 activity was impaired. We isolated seven independent homozygous lines belonging to three different types of mutagenesis events; unfortunately, most of them were in-frame mutants; only one frameshifted *tcr* mutant could be isolated (Figure S4A), which caused a deletion of most of the amino acids at the C-terminal of the TCR protein (Figure S4B). After backcrossing with WT plants, the homozygous line was used as the *TCR* knockout mutant (*tcr*) in this article.

Complementation of *tcr* by *35Spro::TCR*

First, the full-length *TCR* cDNA was amplified using the attB1-TMR-F (GGGGACAAGTTTGTACAAAAAAGCAGGCTAAGAGTAATGATAATACACTGTCCTTCGTCAT) and attB2-TMR-R (GGGGACCACTTTGTACAAGAAAGCTGGGTCTCAGGGACCATAGTCACCATCTC) primers, followed by cloning into the pDONR/Zeo entry vector (Invitrogen). The inserted fragment was isolated and cloned into the pGWB2 destination vector (kindly provided by Dr. Nakagawa of Shimane University, Nakagawa et al., 2007). The constructed *35Spro:TCR*-pGWB2 plasmid was transferred to the *tcr*

mutant using an Agrobacterium-mediated *A. thaliana* transformation method (Bernhardt et al., 2012). Transgenic plants were isolated based on antibiotic resistance, followed by investigation of the levels of the transcript of *TCR* by real-time PCR using the MYZ1-realtimeF (CGGTTATGATGGCTGCTGTG) and MYZ1-realtimeR (TTTGGATTTTGGTCGTTGGA) primers. Two complementing lines (Compl-1 and Compl-2) were isolated independently that exhibited different *TCR* transcript levels (Figure S4C).

Construction of the *pgr5tcr* double mutant

Double mutant *pgr5tcr* lines were produced via artificial pollination between mature pollen from *pgr5* (Munekage et al., 2002) and the young stigma of young buds of *tcr*. The F_1 seeds, which were harvested from the ripe fruit of the double-mutant flowers, were cultivated in soil to obtain F_2 offspring. The homozygosity of the F_2 and F_3 plants with double-gene mutations was assessed by PCR-based genotyping, followed by sequencing of the target genes.

Expression and purification of recombinant TCR

The coding sequence of *TCR* (the 55 N-terminal residues corresponding to the predicted transit peptide were omitted) was amplified by PCR using the pColdI–TCR-F (TCGAAGGTAGGCATATGGCTGCTGTGTCCGTAG) and pCold I-TCR-3R (CGACAAGCTTGAATTTCAGGGACCATAGTCACCATCT) primers. The PCR-amplified fragment was cloned into the pCold-I vector (TAKARA). The integrity of the sequence of the inserted fragment was confirmed by sequencing using the pColdI–TCR-F (TCGAAGGTAGGCATATGGCTGCTGTGTCCGTAG) and M13 (GTTTTGCCAGTCACGAC) primers. The constructed *TCR*-expression plasmid was transferred into *E. coli* BL21 cells (Froger and Hall, 2007) to express His-tagged TCR.

The TCR-expression strain was cultured aerobically in LB medium until OD_{600} = 0.6–0.8, followed by the addition of 2 mM IPTG (to induce the expression of His-tagged TCR) and further incubated at 15°C for 24 h. Cultured cells were collected by centrifugation (9000 rpm at 4°C for 30 min; HITACHI-Himac CR20G). Collected cells were then suspended in binding buffer containing 5 mM imidazole, 0.5 M NaCl, and 20 mM Tris-HCl (pH 8.2), and subjected to sonication (~10 sec for 10 times) on ice in an anaerobic chamber (model A, Coy Laboratory Products, Grass Lake, MI) supplemented with a mixed gas (96 % nitrogen and 4 % hydrogen). Further purification steps were

carried out under the anaerobic conditions. The soluble fraction containing the N-terminal His-tagged TCR recombinant protein was collected after ultracentrifugation (40,000 rpm at 4°C for 1 h; HITACHI-himac CP80WX) and His-tagged TCR was purified using His-Bind Resin (Navogen). His-tagged TCR bound on the column was washed sequentially with 50 ml of binding buffer; 6 ml of a buffer containing 30 mM imidazole, 0.5 M NaCl, and 20 mM Tris-HCl (pH 8.2); and 6 ml of a buffer containing 45 mM imidazole, 0.5 M NaCl, and 20 mM Tris-HCl (pH 8.2). His-tagged TCR was eluted using 2 ml of an elution buffer containing 500 mM imidazole, 0.5M NaCl, and 20 mM Tris-HCl (pH 8.2). The purified TCR was quantified by RC-DC protein assay (BIO-RAD). Absorption spectra were measured using a spectrometer (JASCO V-550) with a screw-capped cuvette to keep anaerobic conditions.

Analysis of the subcellular localization of TCR

A DNA fragment encoding the 64 N-terminal amino acids of TCR (predicted as the plastid transit peptide) was amplified by PCR using the pUC-GFP-F (TACAATTACAGTCGACATGATAATACACTGTCCTTC)and pUC-GFP-R (ATCCTCTAGAGTCGACGTTTTTGGATTTTGGTCGTT) primers and cloned into the *Sal*I-digested pUC18-GFP vector (kindly provided by Dr. Niwa, University of Shizuoka), to generate the in-frame *TCR(1–64 a.a.)-GFP* fusion construct. The *35Spro::TCR(1–64a.a.)-GFP*-pUC18 construct was transiently expressed in onion epidermal cells using a particle gun (PDS-1000He Particle Delivery System, Bio-Rad). The bombarded cells were kept in the dark at 22°C for 16 h, followed by GFP imaging using a fluorescence microscope (ECLIPSE 80i, Nikon).

The full-length *TCR* cDNA was cloned into the pGWB5 destination empty vector (kindly provided by Dr. Nakagawa of Shimane University, Nakagawa et al., 2007), to generate an in-frame *TCR-GFP* fusion construct. The *35Spro::TCR-GFP*-pGWB5 construct was stably expressed in *A. thaliana* via Agrobacterium-mediated transformation (Bernhardt et al., 2012) and antibiotic-resistance screening over 4 to 5 generations. GFP fluorescence signals from mesophyll cells of transgenic plants were observed using a confocal laser scanning microscope (LSM 780 systems, ZEISS) at an excitation wavelength of 488 nm.

To investigate the subcellular localization of TCR, we applied Western blotting using an anti-GFP antibody (Living Colors A.v. monoclonal antibody, JL-8). First, chloroplasts were isolated as described previously (Aronsson and Jarvis, 2002; Kawashima et al., 2017). Second, thylakoid

membranes were isolated after treating chloroplasts with an osmotic shock buffer containing 10 mM Na-pyrophosphate-NaOH (pH 7.8) (Hall et al., 2011), followed by four freeze/thaw cycles. Thylakoid membranes and soluble fractions were separated by centrifugation (2600 $\times$ *g* for 8 min, 4°C), and the membrane fractions were washed with osmotic shock buffer four times. Supernatant fractions were collected by ultracentrifugation (135000 rpm for 1 h, 4°C), to remove membrane contamination. The washed thylakoid membrane fraction was treated with salt-containing buffers (2 M NaBr, 2 M NaSCN, or 0.1 M Na_2CO_3) for 1 h at 0°C (Torabi et al., 2014). Subsequently, all samples were centrifuged as described above and the pellet (thylakoid membranes) and the supernatant (soluble proteins) were applied to SDS–PAGE and Western blotting.

Histochemical analysis of GUS expression

The predicted promoter region of *TCR* (2000 bases upstream of the start codon, ATG) was PCR amplified using the Myz1-Fw (ATGCCTGCAGGTCGACTCCTCTGAATCTAAAAGTC) and Myz1-Rv (ACTGACCCGGGGATCCTATCATTACTCTTGCTGATTT) primers, then cloned into the pBI101 vector (Clontech). The *TCRpro::GUS*-pBI101 construct was transferred into *A. thaliana* Col 0 by Agrobacterium-mediated transformation (Bernhardt et al., 2012). The stable transgenic lines (T_3 generation) that exhibited typical expression of *GUS* were chosen to investigate *TCR* promoter activity. Historical analysis of *GUS* expression was previously described (Vitha et al., 2012). Here, seedlings were germinated for 1, 3, 5, 7, and 17 days; flowers and fruits from 29-day-old transgenic plants grown under constant light conditions were sampled and dipped into the histochemical solution (1 mM X-GLUC, 50 mM phosphate buffer pH 7.2, 0.5 mM $K_3[Fe(CN)_6]$, 0.5 mM $K_4[Fe(CN)]$) overnight at 37°C. The tissues were further washed with 70 % (v/v) ethanol until the chlorophyll was completely removed. The GUS expression patterns were observed using various microscopes (KEYENCE, VB-6010, and Nikon-ECLIPSE-80i).

Transmission electron microscopy

Leaf samples were harvested from 14–21-day-old plants grown under constant light conditions. Leaf samples were cut into small pieces (~3 mm^2 in size), which were treated with a buffer containing 2 % (w/v) paraformaldehyde, 2.5 % (v/v) glutaraldehyde, and 1/15 M phosphate buffer (pH 7.4) for 17 h at 4°C. After washing with 1/15 M phosphate buffer six times, the samples were fixed in a buffer containing 2 % (w/v) osmium tetroxide and 1/15 M phosphate buffer (pH 7.4) for 2 h. The fixed

samples were washed with chilled 8 % (w/v) sucrose twice. Subsequently, the samples were dehydrated in ethanol at increasing concentrations (from 30 % to 100 % (v/v)) and infiltrated with resin for 18 h at room temperature. All samples were placed into molds filled with resin. Polymerization was performed at 65°C for 2 days. Next, the samples were ultra-sectioned and stained, and the ultra-structure of chloroplasts was observed using transmission electron microscopy (TEM).

Measurement of total chlorophyll and carotenoid content

About 15 mg of detached leaves were harvested and homogenized in liquid nitrogen. Total pigments were extracted using 1 ml of chilled 80% (v/v) acetone. The absorption spectra of pigment solutions were measured using a spectrometer (HITACHI-U0080D). Total chlorophyll content was calculated using Arnon's equation (Arnon, 1949; Liang et al., 2017), where *A* was the absorbance of the solution at the designated wavelength:

$$\text{Chlorophyll } a \text{ (}\mu\text{g/ml)} = 12.7A_{663} - 2.69A_{645}$$

$$\text{Chlorophyll } b \text{ (}\mu\text{g/ml)} = 22.9A_{645} - 4.86A_{663}$$

$$\text{Total chlorophyll (mg/ml)} = (20.2A_{645} + 8.02A_{663}) \div 1000.$$

The total carotenoid content was calculated using Lichtenthaler and Wellburn's equation (Lichtenthaler and Wellburn, 1983; Lichtenthaler and Buschmann, 2005), where *A* was the absorbance of the solution at the designated wavelength:

$$\text{Total carotenoid (}\mu\text{g/ml)} = (1000A_{470} - 3.27\text{Chlorophyll } a - 104\text{Chlorophyll } b)/229.$$

Thylakoid extraction and blue native PAGE

This experiment was performed based on a previous publication (Järvi et al., 2011), with slight modifications. Specifically, 4 g of detached leaves was homogenized in 50 ml of grinding buffer containing 330 mM sorbitol, 2 mM EDTA, 1 mM $MgCl_2$, 5 mM ascorbic acid, 0.05 % (w/v) BSA, 10 mM NaF, and 50 mM HEPES/KOH (pH 7.5) using a polytron tissue homogenizer (HITACHI). After filtering through four layers of Miracloth (Merck), the flow-through solution was centrifuged (4000 rpm, 4°C, HITACHI-himac CR20G) for 7 min. The pellet was collected and resuspended in 25 ml of shock buffer

containing 5 mM sorbitol, 5 mM $MgCl_2$, 10 mM NaF, and 50 mM HEPES/KOH (pH 7.5), followed by centrifugation (5000 rpm, 4°C, HITACHI-himac CR20G) for 4 min. The pellet was collected as the thylakoid membrane fraction and resuspended in 2 ml of storage buffer containing100 mM sorbitol, 10 mM $MgCl_2$, 10 mM NaF, and 50 mM HEPES/KOH (pH 7.5).

After measuring chlorophyll content, the thylakoid membrane fractions described above were diluted to 1 mg/ml chlorophyll using ice-cold 25BTH20G buffer containing 20 % (w/v) glycerol, 0.25 mg/ml Pefabloc, and 25 mM Bis-Tris/HCl (pH 7.0). Subsequently, 16 μl of 2 % β-dodecyl maltoside was added to 16 μl of the diluted thylakoid membrane solution. Thylakoid membranes were then solubilized in the dark for 5 min on ice with constant gentle mixing, followed by the removal of traces of insoluble materials by centrifugation (135,000 rpm, 4°C for 20 min, TOMY-Kitman 24). Anode buffer containing 50 mM Bis-Tris/HCl (pH 7.0) and cathode buffer containing 50 mM Tricine, 0.01 % (w/v) Serva Blue, and 15 mM Bis-Tris/HCl were used for electrophoresis. A 3 %–12 % Bis-Tris pre-cast gel (NativePAGE Novex Bis-Tris Gel system) was installed in an XCell SureLock® Mini-Cell apparatus (Invitrogen) before use. Before sample loading into the wells of the gel, thylakoid membrane samples were supplemented with one-tenth volume of ice-cold Serva Blue G buffer containing 0.5 M 6-aminocaproic acid, 30 % (w/v) sucrose, 50 mg/ml Serva Blue G, and 100 mM Bis-Tris/HCl (pH 7.0). Electrophoresis was performed at 4 °C with a gradual increase in the voltage (75 V for 30 min, 100 V for 30 min, 125 V for 30 min, 150 V for 1 h, 175 V for 30 min, and 200 V until the samples reached the bottom of the gel).

SDS–PAGE and Western blotting

Photosynthetic proteins were extracted from chloroplasts that were isolated from *A. thaliana* as described previously (Aronsson and Jarvis, 2002; Kawashima et al., 2017). Total proteins from chloroplasts were precipitated using solution A containing 90 % (v/v) acetone, 10 % (w/v) TCA, and 0.07 % (v/v) 2-mercaptoethanol at –20°C for 60 min. Subsequently, the precipitated proteins were collected by centrifugation (13000 × *g*, 15 min, 4°C, HITACHI-himac CR20G). Pigments were removed from protein samples via washing steps using ice-cold solution B containing 100 % acetone, 0.07 % (v/v) 2-mercaptoethanol, and 2 mM EDTA. Colorless protein fractions were resuspended in buffer E containing 1 % (w/v) SDS, 10 % (v/v) glycerol, 1 mM DTT, and 125 mM Tris-HCl (pH 8.8). Moreover, bacterial proteins were extracted directly from cell pellets by resuspending them in buffer E.

Polyacrylamide gels (10.5 % (w/v) acrylamide, 0.28 % (w/v) BIS, 0.2 % (w/v) SDS, 0.075 % APS (w/v), 0.001 % (v/v) TEMED, and 375 mM Tris-HCl pH 8.8) combined with stacking gels (125 mM Tris-HCl pH 6.8, 3 % (w/v) acrylamide, 0.08 % (w/v) BIS, 0.2 % (w/v) SDS, 0.05 % (w/v) APS, and 0.001 % (v/v) TEMED) were used to separate most of the photosynthetic proteins mentioned in this article. For the analysis of the 6His-TCR recombinant protein, we used a 12 % polyacrylamide gel supplemented with WIDE RANGE gel preparation buffer (4×) (Nacalai Tesque).

Protein samples were mixed with an equal volume of 2× SDS sample buffer containing 125 mM Tris-HCl (pH 6.8), 4 % (w/v) SDS, 20 % (v/v) glycerol, 100 μg/ml bromophenol blue, and 10 % (v/v) 2-mercaptoethanol, followed by boiling at 100°C for 2–5 min before loading onto gels. Electrophoresis was performed using electrophoresis buffer containing 3.03 % (w/v) Tris, 14.31 % (w/v) glycine, and 1% (w/v) SDS in a mini electrophoresis unit (ATTA). The electric current was kept stable at 30 mA for the first 30–45 min and was then changed to 40 mA until the samples reached the bottom of the gel. After electrophoresis, polyacrylamide gels were treated with a CBB staining solution (0.125 % (w/v) CBB R250, 50 % (v/v) methanol, and 10 % (v/v) acetic acid) for at least 30 min, followed by de-staining (25 % (v/v) methanol and 7.5 % (v/v) acetic acid) until the protein bands were observed.

After SDS–PAGE, proteins separated on an unstained polyacrylamide gel were electroblotted onto a polyvinylidene difluoride (PVDF) membrane (Immobilon-P, Merck) using a semi-dry blotting machine (ATTO). Immunodetection was performed using specific antibodies and an ECL Plus Western Blotting Detection System (GE Healthcare). Chemiluminescence signals were captured using the ImageQuant LAS 500 (GE Healthcare). After capture of the Western signals, PVDF membranes were stained with CBB staining solution to observe blotted proteins on the membrane. Specific antibodies against PSBP and PSBR were kindly provided by Dr. Kentaro Ifuku at Kyoto University. Antibodies against PetC, PSBA (D1), PSBS, LHCB6, PSBO, and LHCA3 were purchased from Agrisera. The anti-GFP antibody (Living Colors A.v. monoclonal antibody, JL-8) was purchased from TAKARA.

Measurement of chlorophyll fluorescence

Plants were grown under short-day conditions for 7–8 weeks before measurement. A 3-cm-long rosette leaf was chosen for each measurement. The slow kinetics of chlorophyll fluorescence induction was analyzed using a Dual-PAM-100 measuring system (Walz, Effeltrich, Germany) after 30 min of acclimation of the samples in the dark. The maximum PSII quantum yield (F_v/F_m), Y(II) using

equations defined previously (Butler and Kitajima, 1975; Genty et al., 1989; Bilger and Björkman, 1990; Oxborough and Baker, 1997; Klughammer and Schreiber, 2008; Schreiber and Klughammer, 2008).

To measure the post-illumination chlorophyll fluorescence transient (PIFT), after acclimation in the dark for 15 min, leaf samples were illuminated with strong actinic light (AL, 915 μmol photons m^{-2} s^{-1}) for 2 min or 5 min before the fluorescence induction was observed in the dark within the next 5 min.

Sample sizes (*n*) for all measurements indicate numbers of individuals analyzed.

Measurement of P700

The same plants that were used to measure chlorophyll fluorescence were also employed to assess P700 using a Dual-PAM-100 measuring system (Walz, Effeltrich, Germany). The P700 signal was determined as the difference in absorbance between 875 nm and 820 nm (Klughammer and Schreiber, 2008b). The PSI acceptor-side limitation (Y(NA); a non-photochemical quantum yield measure) was calculated as Y(NA) = ($P_m - P'_m$) / P_m, where P_m is the maximum P700 change from the fully reduced to fully oxidized state and P'_m is the maximum P700 change for a given light state. The PSI donor-side limitation (Y(ND); a non-photochemical quantum yield measure) was calculated as Y(ND) = 1 – P700 red, where P700 red is the fraction of P700 that was reduced in a given state. The photochemical quantum yield of PSI, Y(I), was calculated as Y(I) = 1 – Y(ND) – Y(NA). Sample sizes (*n*) indicate numbers of individuals analyzed.

To measure the reduction of P700 by PC, leaves were illuminated with far-red (FR, 10) light for 30 s, then with saturating pulse (SP, 10) for 3 ms. After turning off SP, decay of P700 absorbance was monitored, which reflected the reduction of $P700^+$ by PC. To monitor the oxidation kinetic of P700 by FR light (10), leaves were dark-acclimated for 30 min before turning on FR light. In another experiment, FR light was kept ON continuously, and leaves were illuminated by the actinic light (AL, 150 μmol photons m^{-2} s^{-1}) for 10 min. After turning off the AL, P700 absorbance is increased due to oxidation of P700 by FR light. These measurements were performed by using Dual-PAM-100 measuring system (Walz, Effeltrich, Germany) with the measuring light (ML) (level 15).

We also used a Joliot Type Spectrometer (JTS-10, BioLogic) to determine the oxidation and reduction of P700 as the difference of absorbance at 705 nm and 740 nm. According to JTS-

10:application note #03 (http://www.bio-logic.info), we set up two different measuring conditions to distinguish the effects of LET and CET on the oxidation of P700 (Joliot and Joliot, 2006). To enhance the linear electron flow, leaf samples were pre-illuminated with red light (150 μmol photons m^{-2} s^{-1}) for 10 min before P700 measurement. In contrast, to enhance the cyclic electron flow, leaf samples were dark-adapted for 10 min and were then irradiated with a saturating pulse for 100 ms before P700 measurement. Far-red (FR, 1400 μmol photons m^{-2} s^{-1}) light was used to induce P700 oxidation.

Electron transfer assay of NADPH, FNR, Fd, and TCR

To measure the ability of Fd to transfer electrons to the TCR recombinant protein, we prepared a reaction solution containing 190 μM His-tagged TCR, 0.5 μM cyanobacterial FNR, 0.5 μM spinach Fd2, 0.5 M NaCl, and 20 mM Tris-HCl (pH 8.2), as described previously (Yonekura-Sakakibara et al., 2000). Subsequently, 1 mM NADPH was mixed with the above reaction solution to start electron transfer from NADPH to FNR, Fd2, and TCR. The absorbance spectra were recorded at room temperature (21–22°C) 5 min and 4 h later using a spectrometer (JASCO-V-550). To avoid the oxidation of TCR, we performed this experiment under anaerobic conditions; we mixed the proteins in a screw-capped cuvette in the anaerobic chamber. When the electron transfer reactions were completed, we exposed the sample to ambient air (opened the cap) for 1–3 min, to observe the re-oxidation of TCR. As a control, we performed the experiment in the absence of Fd.

***In vitro* assay of cyclic electron transport activity of PSI**

This experiment was carried out as described previously (Okegawa et al., 2008), with several modifications. Briefly, chloroplasts were isolated from WT, *tcr*, or *crr4-2* leaves that were harvested from 4-week-old plants that were grown under constant-light conditions (Aronsson and Jarvis, 2002; Kawashima et al., 2017). Subsequently, chloroplasts were ruptured using a chloroplast rupturing buffer containing 7 mM $MgCl_2$, 1 mM $MnCl_2$, 2 mM EDTA, 30 mM KCl, 0.25 mM KH_2PO_4, and 50 mM HEPES/NaOH (pH 8). The ruptured chloroplasts (20 μg of chlorophyll ml^{-1}) were used to monitor Fd-dependent PQ reduction using a DUAL-MINI-PAM system (Walz, Effeltrich, Germany) as the difference in steady-state chlorophyll fluorescence levels. As electron donors, 5 μM spinach Fd (Sigma) and 250 μM β-NADPH (ORIENTAL YEAST Co., LTD, Japan) were used. Antimycin A (10 μM, Funakoshi, Japan) was added to the ruptured chloroplasts before measurements were performed.

Moreover, low measuring light (1 μmol photons m^{-2} s^{-1}) and saturating pulse (3000 μmol photons m^{-2} s^{-1} for 300 ms) conditions were used to measure F_m.

Phylogenetic analysis

The amino acid sequences of TCR homologs were accessed by protein BLAST on NCBI (http://blast.ncbi.nlm.nih.gov). The amino acid sequence alignment was generated and the phylogenetic tree was constructed using MEGA7 (Kumar et al., 2016). The tree was constructed using the neighbor-joining method (Saitou and Nei, 1987) with a bootstrap test of 1000 replicates (Felsenstein, 1985). The tree was drawn to scale, with branch lengths indicated in the same units as those of the evolutionary distances that were used to infer the phylogenetic tree. The evolutionary distances were computed using the JTT matrix-based method (Jones et al., 1992) and are indicated as the number of amino acid substitutions per site. All positions containing gaps and missing data were eliminated.

Identification of photosynthetic proteins by Mass-Spectrometry analysis

Photosynthetic proteins were extracted from chloroplast as mentioned above (See SDS–PAGE and Western blotting in Methods section). The sample preparation for liquid-chromatography tandem-mass spectroscopy-based analysis was described previously (Nojima et al., 2019). Briefly, a volume of protein solution containing 50 μg protein was adjusted to 100 μl by PTS buffer (12 mM sodium deoxycholate, 12 mM sodium N-lauroyl sarcosinate, and 100 mM Tris-HCl pH 9.0). The protein sample was added 1.0 μl of 1 M DTT dissolved in 50 mM ammonium bicarbonate (ABC) buffer, and then the sample was incubated at room temperature (RT) for 30 min. After that, the sample was added 5.0 μl of 1 M 2-idoacetamide (IAA) dissolved in 50 mM ABC buffer, subsequently, incubated at RT for 20 min with shade protection. For limited digestion of proteins into peptide fragments, 400 μl of 50 mM ABC buffer was added to the sample, followed by adding 1.0 μl of Lys-C (Wako, 0.5 μg/μl in 50 mM Tris-HCl pH 8.0), and then incubating at RT for 3 h. Next, 2 μl of trypsin (Promega Trypsin Gold, 0.5 μg/μl in 50 mM acetic acid) was added. Finally, the sample was incubated at 37°C for overnight. Afterwards, PTS was removed from the overnight-incubated sample by the following steps. First, 500 μl of ethyl acetate and then 50 μl of 10 % (v/v) trifluoroacetic acid (TFA) were added to the sample. Second, the ethyl-acetate-containing upper layer was removed from the sample after vortexing for 2 min and centrifuging at 15,700 *g* for 2 min at RT. After solvent removal by a

centrifugal evaporator, the residue was resuspended in 200 μl of buffer A (0.1 % TFA, 2 % acetonitrile). For desalting by using an SDB-XC Stage Tip, the procedure was as follows. The fresh Stage Tip (1 ml tip) was added 1,000 μl of buffer B (0.1 % TFA, 80 % acetonitrile) and centrifuged at 1,500 *g* for 2 min at RT. Next, 1,000 μl of buffer A was added to the Stage Tip, and centrifuged at 1,000 *g* for 2 min at RT; this step was repeated with 500 μl of buffer A. After that, the suspended residue was applied to the Stage Tip and centrifuged at 500 *g* for 3 min at RT. The residue binding to the membrane in the Stage Tip was washed with 1,000 μl and 500 μl of buffer A. Next, the Stage Tip was transferred to a new falcon tube, and then added 300 μl of buffer B, followed by centrifuge at 500 *g* for 3 min at RT. The elution fraction was collected and transferred to a 1.5 ml micro-tube. Next, the residue was collected after 1 h vacuum drying by a centrifugal evaporator, and then resuspended in 50 μl of buffer A. Finally, the sample was centrifuged at 20,000 *g* for 5 min and the supernatant was transfer to a MS vial for the LC-MS/MS measurements (Information Dependent Acquisition (IDA) and SWATH-MS; Gillet et al., 2012) using an Eksigent nanoLC Ultra and TripleTOF 4600 mass spectrometer (AB Sciex, U.S.A.). The settings of the measurement were the same as described in the previous report (Nojima et al., 2019).

Two biological replicates in both WT and *tcr* were prepared and IDA acquisition to construct a SWATH library was conducted once, and SWATH-MS acquisition was conducted three times as technical replicates for each sample. The peptide signal intensities by SWATH-MS acquisition were calculated as an average of the three technical replicates. Only the peptides detected under both conditions were used for the calculation of the foldchange.

ESR analysis

X-band CW-EPR measurements were carried out using a Bruker EMX EPR spectrometer with a super high Q resonator (ER 4122SHQ) and a gas flow temperature control system (ESR900, Oxford Instruments, Oxford, GB.). 0.1 mM TCR in a buffer containing 0.5 M NaCl, and 20 mM Tris-HCl (pH 7.9) was air-oxidized or reduced by 1 mM dithionite (final concentration) for a few minutes, and then packed into synthesized quartz ESR tubes.

Supplemental References

Arnon, D.I. (1949). COPPER ENZYMES IN ISOLATED CHLOROPLASTS. POLYPHENOLOXIDASE IN BETA VULGARIS. Plant Physiol. *24*, 1–15.

Aronsson, H., and Jarvis, P. (2002). A simple method for isolating import-competent *Arabidopsis* chloroplasts. FEBS Lett. *529*, 215–220.

Bernhardt, K., Vigelius, S.K., Linka, N., and Andreas, P.M. (2012). Agrobacterium-mediated *Arabidopsis thaliana* transformation : an overview of T-DNA binary vectors , floral dip and screening for homozygous lines. Endocytobiosis Cell Res. *22*, 19–28.

Bilger, W., and Björkman, O. (1990). Role of the xanthophyll cycle in photoprotection elucidated by measurements of light-induced absorbance changes, fluorescence and photosynthesis in leaves of *Hedera canariensis*. Photosynth. Res. *25*, 173–185.

Butler, W.L., and Kitajima, M. (1975). Fluorescence quenching in Photosystem II of chloroplasts. Biochim. Biophys. Acta *376*, 116–125.

Fauser, F., Schiml, S., and Puchta, H. (2014). Both CRISPR/Cas-based nucleases and nickases can be used efficiently for genome engineering in *Arabidopsis thaliana*. Plant J. *79*, 348–359.

Felsenstein, J. (1985). CONFIDENCE LIMITS ON PHYLOGENIES: AN APPROACH USING THE BOOTSTRAP. Evolution (N. Y). *39*, 783–791.

Froger, A., and Hall, J.E. (2007). Transformation of plasmid DNA into *E. coli* using the heat shock method. J. Vis. Exp. *253*.

Genty, B., Briantais, J.-M., and Baker, N.R. (1989). The relationship between the quantum yield of photosynthetic electron transport and quenching of chlorophyll fluorescence. Biochim. Biophys. Acta *990*, 87–92.

Gillet, L.C., Navarro, P., Tate, S., Röst, H., Selevsek, N., Reiter, L., Bonner, R., and Aebersold, R. (2012). Targeted data extraction of the MS/MS spectra generated by data-independent acquisition: A new concept for consistent and accurate proteome analysis. Mol. Cell. Proteomics *11*, 1–17.

Griffiths, A.J., Miller, J.H., Suzuki, D.T., Lewontin, R.C., and Gelbart, W.M. (2000). Introduction to Genetic Analysis, 7th editio. ed. New York: W. H. Freeman.

Hall, M., Mishra, Y., and Schröder, W.P. (2011). Preparation of stroma, thylakoid membrane, and

lumen fractions from *Arabidopsis thaliana* chloroplasts for proteomic analysis. Methods Mol. Biol. *775*, 207–222.

Ifuku, K., Endo, T., Shikanai, T., and Aro, E.M. (2011). Structure of the chloroplast NADH dehydrogenase-like complex: Nomenclature for nuclear-encoded subunits. Plant Cell Physiol. *52,* 1560–1568.

Järvi, S., Suorsa, M., Paakkarinen, V. and Aro, E.-M. (2011). Optimized native gel systems for separation of thylakoid protein complexes: novel super- and mega-complexes. Biochem. J. *439*, 207–214.

Joliot, P., and Joliot, A. (2006). Cyclic electron flow in C3 plants. Biochim. Biophys. Acta *1757*, 362–368.

Jones, D.T., Taylor, W.R., and Thornton, J.M. (1992). The rapid generation of mutation data matrices from protein sequences. Bioinformatics *8*, 275–282.

Kawashima, R., Sato, R., Harada, K., and Masuda, S. (2017). Relative contributions of PGR5- and NDH-dependent photosystem I cyclic electron flow in the generation of a proton gradient in Arabidopsis chloroplasts. Planta *246*, 1045–1050.

Klughammer, C., and Schreiber, U. (2008a). Complementary PS II quantum yields calculated from simple fluorescence parameters measured by PAM fluorometry and the Saturation Pulse method. PAM Appl. Notes *1*, 27–35.

Klughammer, C., and Schreiber, U. (2008b). Saturation Pulse method for assessment of energy conversion in PS I. PAM Appl. Notes *1*, 11–14.

Kono, M., Yamori, W., Suzuki, Y., and Terashima, I. (2017). Photoprotection of PSI by far-red light against the fluctuating light-induced photoinhibition in Arabidopsis thaliana and field-grown plants. Plant Cell Physiol. *58*, 35–45.

Kumar, S., Stecher, G., and Tamura, K. (2016). MEGA7: Molecular Evolutionary Genetics Analysis Version 7.0 for Bigger Datasets. Mol. Biol. Evol. *33*, 1870–1874.

Labun, K., Montague, T.G., Gagnon, J.A., Thyme, S.B., and Valen, E. (2016). CHOPCHOP v2: a web tool for the next generation of CRISPR genome engineering. Nucleic Acids Res. *44*, W272–W276.

Liang, Y., Urano, D., Liao, K.-L., Hedrick, T.L., Gao, Y. and Jones, A.M. (2017). A nondestructive

method to estimate the chlorophyll content of Arabidopsis seedlings. Plant Methods *13*, 26.

Lichtenthaler, H., and Wellburn, A. (1983). Determinations of total carotenoids and chlorophyll *a* and *b* of leaf extracts in different solvents. Biochem. Soc. Trans. *11*, 591–592.

Lichtenthaler, H.K., and Buschmann, C. (2005). Chlorophylls and Carotenoids: Measurement And Characterization by UV-VIS Spectroscopy. Handb. Food Anal. Chem. *2–2*, 171–178.

Munekage, Y., Hashimoto, M., Miyake, C., Tomizawa, K.-I., Endo, T., Tasaka, M., and Shikanai, T. (2004). Cyclic electron flow around photosystem I is essential for photosynthesis. Nature *429*, 579–582.

Munekage, Y., Hojo, M., Meurer, J., Endo, T., Tasaka, M., and Shikanai, T. (2002). PGR5 is involved in cyclic electron flow around photosystem I and is essential for photoprotection in Arabidopsis. Cell *110*, 361–371.

Nakagawa, T., Kurose, T., Hino, T., Tanaka, K., Kawamukai, M., Niwa, Y., Toyooka, K., Matsuoka, K., Jinbo, T., and Kimura, T. (2007). Development of series of gateway binary vectors, pGWBs, for realizing efficient construction of fusion genes for plant transformation. J. Biosci. Bioeng. *104*, 34–41.

Nojima, T., Niwa, T., and Taguchi, H. (2019). Proteome analysis of phase-separated condensed proteins with ionic surfactants revealed versatile formation of artificial biomolecular condensates. Biomacromolecules *20*, 539–545.

Okegawa, Y., Kagawa, Y., Kobayashi, Y., and Shikanai, T. (2008). Characterization of factors affecting the activity of photosystem I cyclic electron transport in chloroplasts. Plant Cell Physiol. *49*, 825–834.

Oxborough, K., and Baker, N.R. (1997). Resolving chlorophyll *a* fluorescence images of photosynthetic efficiency into photochemical and non-photochemical components – calculation of *qP* and *Fv'*/*Fm'* without measuring *Fo'*. Photosynth. Res. *54*, 135–142.

Rumeau, D. (2004). New subunits NDH-M, -N, and -O, encoded by nuclear genes, are essential for plastid Ndh complex functioning in higher plants. Plant Cell *17*, 219–232.

Saitou, N., and Nei, M. (1987). The neighbor-joining method: a new method for reconstructing phylogenetic trees. Mol. Biol. Evol. *4*, 406–25.

Schiml, S., Fauser, F., and Puchta, H. (2014). The CRISPR/Cas system can be used as nuclease for in planta gene targeting and as paired nickases for directed mutagenesis in Arabidopsis resulting in heritable progeny. Plant J. *80*, 1139–1150.

Schreiber, U., and Klughammer, C. (2008). Non-photochemical fluorescence quenching and quantum yields in PS I and PS II: Analysis of heat-induced limitations using Maxi-Imaging- PAM and Dual-PAM-100. PAM Appl. Notes *1*, 15–18.

Stemmer, M., Thumberger, T., del Sol Keyer, M., Wittbrodt, J., Mateo, J.L. and Henrich, T. (2015). CCTop: An Intuitive, Flexible and Reliable CRISPR/Cas9 Target Prediction Tool. PLoS One *10*, e0124633.

Torabi, S., Umate, P., Manavski, N., Plöchinger, M., Kleinknecht, L., Bogireddi, H., Herrmann, R.G., Wanner, G., Schröder, W.P. and Meurer, J. (2014). PsbN is required for assembly of the Photosystem II reaction center in Nicotiana tabacum. Plant Cell *26*, 1183–1199.

Vitha, S., Benes, K., Phillips, J.P., Gartland, K.M.A., Beneš, K., Phillips, J.P., and Gartland, K.M.A. (2012). Histochemical GUS Analysis, in: Agrobacterium Protocols. Humana Press, New Jersey, pp. 185–194.

Xie, K., Zhang, J., and Yang, Y. (2014). Genome-wide prediction of highly specific guide RNA spacers for CRISPR–Cas9-mediated genome editing in model plants and major crops. Mol. Plant *7*, 923–926.

Xu, D., and Zhang, Y. (2013). Toward optimal fragment generations for ab initio protein structure assembly. Proteins Struct. Funct. Bioinforma. *81*, 229–239.

Xu, D., and Zhang, Y. (2012). Ab initio protein structure assembly using continuous structure fragments and optimized knowledge-based force field. Proteins *80*, 1715-1735.

Yonekura-Sakakibara, K., Onda, Y., Ashikari, T., Tanaka, Y., Kusumi, T., and Hase, T. (2000). Analysis of reductant supply systems for ferredoxin-dependent sulfite reductase in photosynthetic and nonphotosynthetic organs of maize. Plant Physiol. *122*, 887–894.